PH.D. THESIS

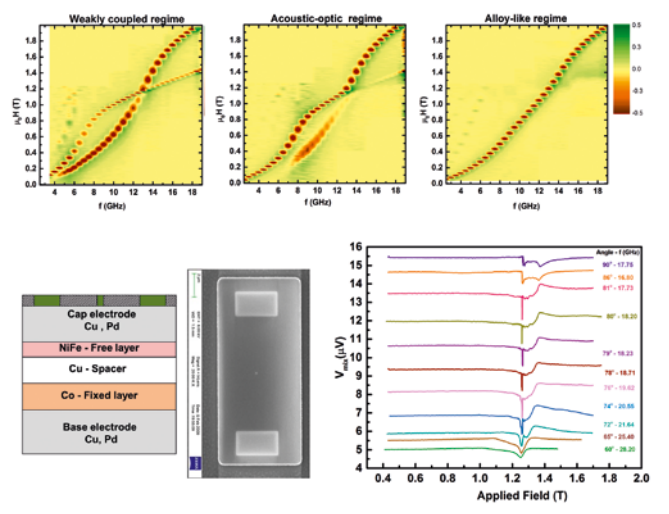

Magnetodynamics of Pseudo-Spin-Valves

Investigated Using Coplanar Wave Guide and Spin-torque Ferromagnetic Resonance Techniques

Masoumeh Fazlali

DEPARTMENT OF PHYSICS

UNIVERSITY OF GOTHENBURG

Magnetodynamics of pseudo-spin-valves investigated using coplanar wave guide and spin-torque ferromagnetic resonance techniques

Coupled and uncoupled trilayers, coincidence point resonance, and the high Q-factor peak at the resonance of coupled layers

Masoumeh Fazlali

Thesis for the degree of
Doctor of Philosophy in Natural Science, specializing in Physics

UNIVERSITY OF GOTHENBURG

June 2017

‘Our job in physics is to see things simply, to understand a great many complicated phenomena in a unified way, in terms of a few simple principles.’ Steven Weinberg

ISBN: 978-91-629-0226-1(printed)
ISBN: 978-91-629-0225-4 (pdf)

Printed by Kompendiet, Gothenburg, 2017

Abstract

Nanocontacts (NCs) on magnetic multilayers are well-known in the implementation of spin torque oscillators, due to their frequency tunabilities that range from tens of GHz for spin-wave bullets and droplet-based oscillators to deeply sub-GHz bands for vortex-based oscillators. Moreover, they can generate a wide range of highly nonlinear localized and propagating SW modes for use in magnonics. However, I have found that most studies have focused on the application point of view, and there are large unexplored areas in the fundamental physics of these structures.

This thesis focuses on exploring the magnetization dynamics of NCs on Co/Cu/Py pseudo-spin-valves (pSV) using the spin torque ferromagnetic resonance technique (ST-FMR) and the broadband conventional FMR technique. The thesis is thematically divided into two parts.

In the first part, which includes two papers, I utilize the ST-FMR technique to excite and detect spin-wave resonance (SWR) spectra in tangentially magnetized NCs.

i) First, the origin of the magnetodynamics of the detected spectra is explored. I find that the NC diameter sets the mean wavevector of the exchange-dominated spin wave, in good agreement with the dispersion relation. The micromagnetic simulations suggest that the rf Oersted field in the vicinity of the NC plays the dominant role in generating the spectra observed.

ii) This work is followed by another work that involves tuning the exchange-dominated spin wave using lateral current spread. To this end, different thicknesses of the Cu bottom layer are used to control the lateral current spread.

In the second part, which includes three manuscripts, I explore the coupling between two ferromagnetic layers through different thickness of Cu interlayers.

i) First, I study the nature of coupling in tangentially magnetized blanket trilayer Co/Cu/Py with different thickness of Cu of 0–40 Å by using broadband conventional ferromagnetic resonance. I observe the oscillatory behavior of the exchange constant versus the interlayer thickness, showing an RKKY type of interaction, although the exchange constant (J) is always positive. Three different regimes corresponding to alloy-like coupling ($t_{\mathrm{Cu}} \leq 5A$), strong FM coupling (the acoustic–optic regime, $t_{\mathrm{Cu}} = 7.5$, 8.1, and 16.2), and weak FM coupling (overall FM ordering, Cu $\geq$ 8.8) is found. Furthermore, the experimental results show a saturated field, especially in the Co shift to higher values in samples with stronger interlayer exchange coupling (IEC). Finally, in the case of the samples corresponding to the collective regime, there is a critical field below which just

one acoustic mode exists. This mode below the critical field shows very low linewidth, compared to single-layer or alloy-like regime samples. These results demonstrate that, by using the strength of the IEC, it is possible to engineer a cut-off frequency in magnetic trilayers, below which the spin pumping is turned off.

ii) Second, knowing the fact that Co and NiFe have very different Larmor frequencies in the in-plane applied field (except very low f–H conditions), their f–H dependencies change at higher angles of the applied field. I focus on the collective dynamics of the FM/N/FM system, when the FMR frequencies of the separate layers form a crosspoint (CP) at a particular value of the applied magnetic field, and are substantially different otherwise. One of the CPs takes place when the applied field makes an 8 degree angle normal to the film at $H = 11800$ Oe, $f = 13$ GHz. Here again, I observe substantially different types of field spectra as a function of Cu thickness, but the borders of regimes are shifted. When the Cu thickness is $t < 8.5$ Å, the trilayer structure has only one mode, that of the alloy-like behavior. For $t = 8.8$ and 16.6 Å, the structure shows the collective dynamics of both layers, which modify the FMR frequencies in the whole range of the applied field. For the intermediate value of $t = 10$ Å and the large values of $t = 20$ and $t = 40$ Å, the Co and NiFe layers demonstrate individual dynamics with low coupling. Such a periodical dependence of the coupling strength on the spacer thickness confirms the previous work's conclusion on the strong RKKY interlayer interaction. However, the shift of the regime borders for a typical sample in the two studies shows how the exchange coupling (J) relies on the angle between the magnetization of the two layers and, as a result, on the direction of the applied field. In the case of strong coupling ($t = 8.8$, $t = 16.6$ Å), a broad bandgap (> 1 GHz) is formed at the field spectra CP. At lower values of the applied field, the acoustic and optical modes have a strong blue frequency shift as compared to the uncoupled trilayer structure. This shift is especially large at $H = 0$ for the optical mode (~ 4 GHz).

iii) Third, I studied the NC device with a trilayer pseudo-spin-valve with two different interlayer thicknesses ($t_{\mathrm{Cu}} = 20$ Å and $t_{\mathrm{Cu}} = 80$ Å) at the same field angle used in the previous work, $\theta = 82°$. The aim of this work is to study the weakly coupled regime ($t_{\mathrm{Cu}} = 20$ Å) and to compare it with the almost uncoupled regime ($t_{\mathrm{Cu}} = 80$ Å) in the vicinity of the CP. Surprisingly, it is observed that sharp (high Q-factor) modes appear in the vicinity of the CP in the weakly coupled regime. It seems that the coupling of FM layers near the CP point tends to suppress all the spectra, except over a very small range of f–H, which leads to these sharp peaks. One possible explanation for this phenomenon is the Slonczewski mode nucleated by the spin pumping from Co to Py layer.

Dedication

This dissertation is dedicated to my loving parents, who showed me the most basic rule of the world, beyond all sciences: 'The foundation of the universe is love.'

Acknowledgments

First and foremost, I am deeply grateful to my advisor, Professor Johan Åkerman. Being a member of the Applied Spintronics group has been a milestone in my career that has led me to explore my professional capabilities. Professor Åkerman's expertise, generous scientific expenditure, and management of such a large group made it possible for me to focus on the topics that interested me. In addition to his scientific knowledge, I have learned from him how to work efficiently and systematically, and how to bring ideas efficiently to publication. I have learned from him how to keep up with the latest software, techniques, and technologies, so as to increase the value of the work, and how to stay up to date by attending conferences and daily literature reviews.

I appreciate my coadvisor, Dr. Martina Ahlberg, for all her support and collaborative approach. She was my mentor during the extremely busy final year of my PHD studies, where she worked with me on the analysis of data, and responded with endless patience to my questions. I would also like to thank Dr. Randy K. Dumas for helping me to learn measurement techniques, running a fruitful course on applied spintronics, and as the senior author who helped me write my first paper.

My sincere thanks go to Professor Pranaba Muduli at the Indian Institute of Technology for his kind support in solving equipment software issues during his annual visit at GU. I am also deeply grateful to Professor Mattias Goksör, the current head of the Physics Department at GU, for leading a great department with the strong support of students in every way. Special thanks are due to Professor Jonas Fransson at Uppsala University, regarding fruitful discussions for the last section of my thesis.

I would like to express my sincere gratitude to my collaborators in Professor Peter Svedlindh's group for the pleasure of contribution in their excellent publications. A big thanks also goes to Dr. Philipp Dürrenfeld for his endless support in the beginning, especially in training me in nanofabrication, Dr. Ezio Iacocca, Dr. Roman Khymyn, and Dr. Mykola Dvornik for their fruitful discussions, and special thanks to Mykola Dvornik for his simulation work on my first manuscript.

I should also thank Maria Siirak, Clara Wilow Sundh and Bea Augustsson for all of their administrative support during the four years of my PhD. Thank you so much for your excellent work!

Turning into my wonderful colleagues and friends in our group, I appreciate M. Balinsky, M. Haidar, A. Awad, M. Ranjbar, S.R. Etesami, H. Fulara, M. Zahedinejad, A. Hushang, J. Yue, Y. Yin, Sh. Muralidhar, S. Chung, A. Banuazizi, H. Mazraati, and all the Applied

Spintronics group members who have assisted me over these years.

Finally, I would like to thank my father and two brothers, Mohammad and Reza. Without their love and support over the years, none of this would have been possible. They have been always there for me and I am thankful for everything they have helped me to achieve.

Publications

List of manuscripts and papers included in this thesis:

I **M. Fazlali**, M. Dvornik, E. Iacocca, P. Dürrenfeld, M. Haidar, J. Åkerman, and R. K. Dumas,
"Homodyne-detected ferromagnetic resonance of in-plane magnetized nanocontacts: Composite spin-wave resonances and their excitation mechanism",
Physical Review B **93**(2016), 134427.

II **M. Fazlali**, S. A. H. Banuazizi, M. Dvornik, M. Ahlberg, S. R. Sani, S. M. Mohseni, and J. Åkerman
"Tuning exchange-dominated spin-waves using lateral current spread in nanocontact spin-torque nano-oscillators",
manuscript in preparation for Applied Physics Letters.

III **M. Fazlali**, M. Ahlberg, M. Dvornik, and J. Åkerman
"Tunable spin pumping in exchange coupled magnetic trilayers",
manuscript in preparation for Physical Review Letters.

IV **M. Fazlali**, M. Ahlberg, R. Khymyn, and J. Åkerman
"From individual to collective behavior in the multilayered magnetic structure in the vicinity of resonance coincidence point. Broadband FMR measurements of the Co/Cu/Py trilayers"
manuscript in preparation for Physical Review B.

V **M. Fazlali**, M. Ahlberg, M. Dvornik, and J. Åkerman
"Effect of the microwave current on resonances of coupled Py/Cu/Co trilayers in oblique magnetic fields",
manuscript in preparation for Nature communication.

List of papers which I have contributed to, but are not included in this thesis:

VI A. Houshang, **M. Fazlali**, S. R. Sani, P. Dürrenfeld, E. Iacocca, J. Åkerman, and R. K. Dumas
"Effect of sample fatigue on the synchronization behaviour on multiple nanocontact spin torque oscillator" ,
IEEE Magnetics Letters, **5** (2014), 3000404.

VII A. Kumar, S. Akansel, H. Stopfel, **M. Fazlali**, J. Åkerman, R. Brucas, and P. Svedlindh

"Spin transfer torque ferromagnetic resonance induced spin pumping in the Fe/Pd bilayer system",

Physical Review B **95** (2017), 064406.

Declaration

This thesis is a presentation of my original research work. It is the result of cooperative efforts, and I am grateful for the contributions and endless support of my colleagues. The work was performed under the guidance of Professor Johan Åkerman, at the Department of Physics, University of Gothenburg, Sweden. The contributions of the author (MF) to the appended papers are as follows:

Paper I : MF performed the measurement, contributed to the analytical approach with MD and wrote the first manuscript (except simulation and discussion sections).

Paper II : MF performed the measurement, designed the analytical approach, and wrote the first manuscript.

Paper III : MF fabricated the samples, performed the measurement, and contributed to the analysis with MA.

Paper IV : MF fabricated the samples, performed the measurement, contributed to the analysis with MA and RK, and wrote the first manuscript.

Paper V : MF fabricated the devices, performed the measurement, set meetings with JF regarding Fano discussions, contributed to the analysis with MA, MD, and wrote the first manuscript.

Paper VI : MF performed ST-FMR measurements and ST-FMR analysis.

Paper VII : MF contributed to the fabrication of devices and reviewed the paper.

Masoumeh Fazlali

Contents

Chapter 1

Basics

1.1 Spin waves

1.1.1 The concept of spin waves

In 1930, the concept of spin waves as elementary excitations that occur in ordered magnetic materials was introduced by Bloch [1]. He was the first to present the idea that the dynamic excitations of the spin system of magnetic crystals had the character of the collective precession of the individual spins, which can be represented as a propagating wave. When the quantum-mechanical nature of the spins is taken into account, the corresponding quasiparticles that arise from the quantization of the spin waves are called magnons.

In fact, various alternative approaches to spin wave theory can be followed. These mathematical frameworks include semiclassical approaches, such as that due to Heller and Kramers [2] (Fig. 1-1) and quantum-mechanical approaches. The semiclassical approach is particularly helpful in gaining physical interpretations.

Spin waves at low temperatures behave, to a good approximation, as noninteracting elementary excitations with boson-like characteristics. However, it should be noted that spin waves are not exact normal modes of the system, and this leads to an interaction between them and also to other nonlinear effects [5]. The path of the discovery of experimental evidence for spin waves can be found, for example, in Refs. [3, 4].

1.1.2 Spin waves in infinite media (without boundary conditions)

Maxwell's equations for magnetoquasistatics reduce to

$$\nabla \times h = 0 \tag{1.1}$$

$$\nabla . b = 0$$

$$\nabla \times e = i\omega b.$$

For a magnetized film, we have

$$b = \overline{\mu} . h \tag{1.2}$$

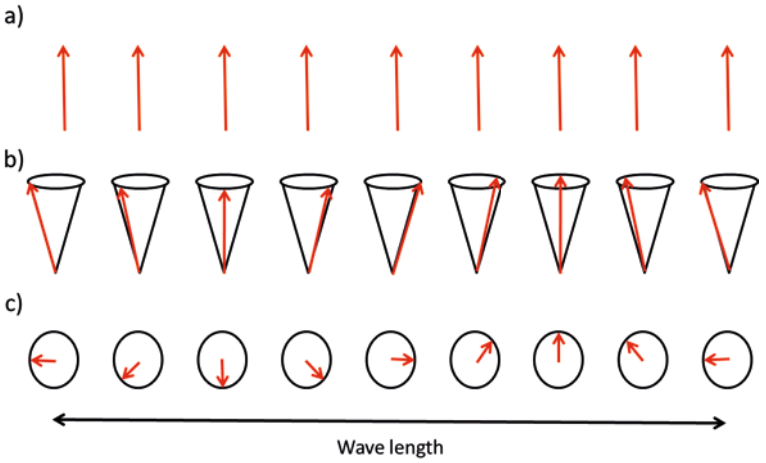

Figure 1.1: Semiclassical representation of a spin wave in a ferromagnet: (a) ground state with magnetization vectors parallel: $M(t=0) = M_0\vec{k}$; (b) perspective view of a spin wave of precessing spin vectors: $M(t) = M_z\vec{k} + M_r e^{i\omega t}\vec{r}$; (c) top view: the oscillating component of the magnetization vector, $M_r e^{i\omega t}\vec{r}$.

$$\overline{\mu} = \mu_0(I + \overline{\chi}),$$

where $\overline{\mu}$ is the permeability tensor.

$$\overline{\chi} = \begin{bmatrix} \chi & i\chi_a \\ -i\chi_a & \chi \end{bmatrix} \tag{1.3}$$

$$\chi = \frac{\omega_M \omega_H}{\omega_H^2 - \omega^2}, \qquad \chi_a = \frac{\omega_M \omega}{\omega_H^2 - \omega^2}, \qquad \omega_H = \gamma\mu_0 H_0, \qquad \omega_M = \gamma\mu_0 M_0.$$

Assuming the bias field (H_0) lies along the z-direction, combining the equations leads to

$$(1+\chi)\left[\frac{\partial^2 A(r)}{\partial x^2} + \frac{\partial^2 A(r)}{\partial y^2}\right] + \frac{\partial^2 A(r)}{\partial z^2} = 0. \tag{1.4}$$

Equation (1.4) is called Walker's equation and is the basic equation for magnetostatic modes in homogeneous media [5]. It is well-known that any excitation, such as spin waves, must satisfy the symmetry requirements in accordance with Bloch's Theorem [6], which states that the variable A(r) describing the spin-wave amplitude must have the general form

$$A(\mathrm{r}) = exp(i\mathrm{k}.\mathrm{r})\ U_k(\mathrm{r}). \tag{1.5}$$

Here, k is a wavevector in the Brillouin zone corresponding to the reciprocal lattice of the crystal, and U_k(r) is a periodic function of the potential of the crystal lattice. The overall phase vector $exp(i$k.r) gives a plane-wave variation to A(r). For a spin wave, A(r) is the appropriate component of spin of the magnetization. The spin-wave energy is denoted by $\hbar\omega$(k) where ω(k) is the excitation frequency [7].

If the propagation angle with respect to the z-axis (also the direction of the DC bias field) is θ, then putting (1.5) into Equation (1.4) gives:

$$\chi \sin^2 \theta = 1. \tag{1.6}$$

This can be expressed explicitly in terms of the frequency using Equation (1.3) for χ:

$$\omega = \left[\omega_H(\omega_H + \omega_M \sin^2 \theta)\right]^{1/2}. \tag{1.7}$$

This shows the independence of k from the magnitude: that is, waves at this frequency can have any wavelength. This happens because we did not assume any boundary conditions. In real experiments on spin waves, samples of finite size are always used. Taking into account the boundary conditions on the film surfaces leads to changes in the spin-wave spectrum: first there is a discrete spin-wave spectrum consisting of separate dispersion branches corresponding to spin waves with different distributions of variable magnetization across the film thickness. Second, the spin-wave eigenfrequencies depend on the magnitude of the wavevector.

1.1.3 Types of spin waves in ferromagnetic films (with boundary conditions)

The magnitude of the wavevector k of a spin wave identifies its properties. The dipole–dipole interaction plays a fundamental role in the propagation of relatively long-wavelength spin waves with wavenumbers $|k| \leq 10^7$ m^{-1}, where the wavelength may be comparable to the characteristic size of the ferromagnetic sample. Such waves are customarily referred to as magnetostatic spin waves [7]. For short-wavelength spin waves (with $|k| > 10^8$ m^{-1}), the exchange interaction plays a fundamental role. The exchange region includes most of the Brillouin zone (a zone-boundary wavevector has a magnitude of about 10^{10} m^{-1}). In order to emphasize this distinction, we will refer to such waves as exchange spin waves. Finally, there is an intermediate region, referred to as the dipole-exchange region, typically corresponding to 10^8 m^{-1} $> |k| >$ 10^7 m^{-1}, in which the dipole and exchange terms are comparable. At very small values of $|k|$, the full form of Maxwell's equations should be used; this region is called the electromagnetic region. Table 1.1 summarizes different regions of spin waves.

1.1.4 Magnetostatic spin waves

Magnetostatic spin waves (MSWs) are anisotropic due to the anisotropic nature of dipolar interaction. MSWs in a normally magnetized film are called forward-volume magnetostatic

Region	Wavevector range
Exchange region	$\lvert k\rvert > 10^8$ m^{-1}
Dipole-exchange region	10^8 m$^{-1} > \lvert k\rvert > 10^7$ m^{-1}
Magnetostatic region	10^7 cm$^{-1} > \lvert k\rvert > 3 \times 10^3$ m^{-1}
Electromagnetic region	$\lvert k\rvert < 3 \times 10^3$ m^{-1}

Table 1.1: Different regions of spin-wave excitations in terms of the magnitude $|k|$ of their wavevector. The numbers are approximate for ferromagnetic materials. For comparison, a Brillouin zone boundary wavevector is approximately of magnitude 10^{10} m^{-1} [8].

waves (FVMSWs). MSWs in an in-plane magnetized magnetic film are classified in two ways, depending on the angle between k and the applied field (H). Waves propagating along the applied field are called backward-volume magnetostatic waves (BVMSWs), while waves propagating transverse to the applied field are called magnetostatic surface waves (MSSWs, also known as Damon–Eshbach waves) [9].

The dispersion relation for FVMSWs in a normally magnetized film is

$$\omega^2 = \omega_H \left[\omega_H + \omega_M \left(1 - \frac{1 - e^{-kd}}{kd}\right)\right]. \tag{1.8}$$

The phase and group velocities are both in the same direction. Waves with this characteristic are called forward waves. In addition, the wave amplitude is distributed sinusoidally through the volume of the film. Because of these two characteristics, these are called magnetostatic forward-volume spin waves (Fig. 1.2).

The dispersion relation for BVMSWs in a tangentially magnetized film is:

$$\omega^2 = \omega_H \left[\omega_H + \omega_M \left(\frac{1 - e^{-kd}}{kd}\right)\right]. \tag{1.9}$$

The phase and group velocities here point in opposite directions. A wave with this property is called a backward wave; the wave amplitude is then distributed sinusoidally through the volume of the film. The term magnetostatic backward-volume wave follows from these two characteristics (Fig. 1.2). The dispersion relation for MSSWs in a tangentially magnetized film is:

$$\omega^2 = \omega_H(\omega_H + \omega_M) + \frac{\omega_M^2}{4}\left[1 - e^{-2kd}\right]. \tag{1.10}$$

The phase and group velocities point in the same direction, and thus this mode is a forward wave. The wave amplitude is not distributed periodically through the film thickness, but instead decays exponentially from the surfaces of the film. Because of this last observation, these modes are called magnetostatic surface waves (Fig. 1.2). The dispersion relation of all three types of magnetostatic waves for the sample NiFe with $t = 100$ nm are demonstrated in Figure 1.2.

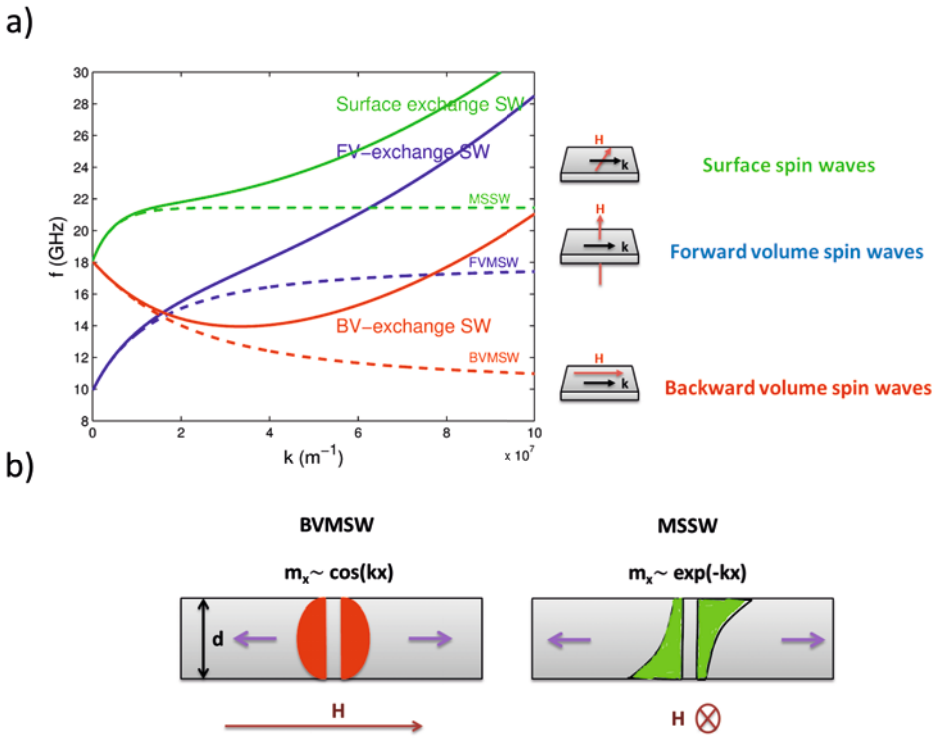

Figure 1.2: (a) Dispersion relation of different types of spin waves for FMR resonance condition at $f = 18$ GHz in NiFe film with a thickness of $t = 100$ nm. The solid and dashed lines respectively show the dispersion relation, with and without the exchange term. (b) Dynamic magnetization profile of modes.

1.1.5 Exchange spin waves

In the presence of exchange, h is obtained from m using the matrix differential $\overline{A_{op}}$:

$$h = \overline{A_{op}}.m, \tag{1.11}$$

where

$$\overline{A_{op}} = \frac{1}{\omega_M}\begin{bmatrix} \omega_H - \omega_M\lambda_{ex}\nabla^2 & i\omega \\ -i\omega & \omega_H - \omega_M\lambda_{ex}\nabla^2 \end{bmatrix}.$$

For uniform plane wave propagation, $A(\mathrm{r}) = exp(i\mathrm{k}.\mathrm{r})\ U_k(\mathrm{r})$, the operator ∇^2 can be replaced by the factor k^2. Since the exchange term $\omega_M\lambda_{ex}k^2$ appears everywhere with ω_H, it follows that the effects of exchange can be added to the previous magnetostatic plane

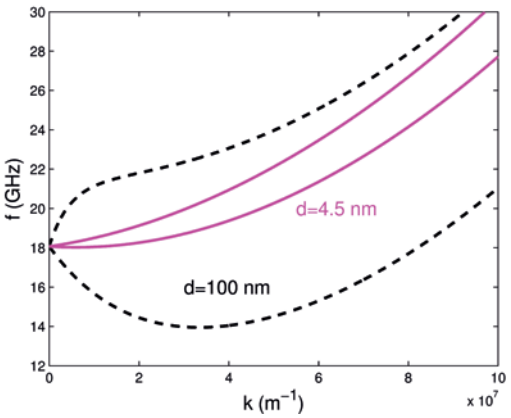

Figure 1.3: Comparison between dispersion relations of in-plane magnetized NiFe samples with $d = 100$ nm and $d = 4.5$ nm shown by dashed lines and solid lines, respectively.

wave analysis by simply replacing ω_H by $\omega_H + \omega_M \lambda_{ex} k^2$. Figure 1.2 (a) shows the effect of adding the exchange term to the dispersion relation of all three types of magnetostatic spin wave.

Figure 1.3 shows the dispersion relations of tangentially magnetized NiFe film with two different thickness. From this plot, it can be seen that for ultrathin films, the critical wavevector that defines the borders between the magnetostatic regime and the exchange regime goes to zero—i.e., the exchange interaction dominates the magnetodynamics in tangentially magnetized ultrathin films. As a result, for ultrathin films, the dispersion relations simply follow equation (1.12).

$$\omega = \left[\left(\omega_{\mathrm{H}}^{\mathrm{SWR}} + \omega_M \left(\lambda_{ex} k \right)^2 \right) \times \left(\omega_{\mathrm{H}}^{\mathrm{SWR}} + \omega_M + \omega_M \left(\lambda_{ex} k \right)^2 \right) \right]^{1/2} \tag{1.12}$$

where $\lambda_{ex} = \sqrt{2A/\mu_0 M_s^2}$ and k are the exchange length and the spin wave resonance (SWR) wavevector, respectively. Any physical confinement or quasiconfinement (D') can lead to discrete values of $k = n\pi/D'$, which for the first order approximates to $k = \pi/D'$.

The study of exchange spin waves is interesting both from the applications and fundamental points of view. Along with elastic and magnetostatic waves, exchange spin waves are "slow" waves—that is, their phases and group velocities are small compared to the velocity of an electromagnetic wave (Table 1.1). This is why exchange spin waves are promising candidates for use in making small microwave engineering elements, similar to those that use surface acoustic waves and magnetostatic spin waves. On the other hand, the wavelength of exchange spin waves is comparable to that of sound and light waves; These spin waves could thus be important objects and instruments for investigating the interactions

between waves of various types. The experimental study of exchange spin waves, which started more than fifty years ago, involves the use of three basic experimental methods: the study of spin-wave resonance spectra in thin ferromagnetic films, the measurement of frequency and field dependencies of the threshold for parametric excitation of exchange spin waves, and the investigation of the scattering of light by thermal or parametrically excited magnons [7, 10].

1.1.6 Slonczewski propagating spin-wave

Types of spin waves, including magnetostatics and magnetodynamics, have been generally discussed. In 1996, Slonczewski showed theoretically[11] and later confirmed experimentally [12, 13, 14] that a sufficiently large electric current passing through a trilayer ferromagnetic/nonmagnetic/ferromagnetic (F/N/F) with noncollinear magnetizations can transfer vector spin between the magnetic layers, exciting precession of the layer magnetizations, and as a result stimulating the emission of propagating spin waves (exchange spin waves). In 2007, Slavin et al.[15] showed in the case of nanocontact geometry, the direction of the external bias magnetic field and the variation in the magnetization angle can lead to a qualitative change in the nature of the excited spin wave modes.

In the case of a normally magnetized film, the frequency of the excited spin wave is always larger than the frequency of the FMR mode of the free magnetic layer:

$$\omega(k) = \omega_H + \omega_M \left(\lambda_{ex} k\right)^2 + Na^2 \tag{1.13}$$

where N is the coefficient of a nonlinear frequency shift and in this geometry is always positive, $N > 0$; a is the amplitude of the excited spin wave mode. In the case of an in-plane magnetized nanocontact, the coefficient of the nonlinear frequency shift is negative, $N < 0$, and therefore has the opposite sign of the exchange term. This geometry can thus support a strongly localized nonpropagating spin wave mode of a solitonic type.

1.1.7 Techniques for exciting spin waves

Initially, the first experimental evidence of spin waves came from the measurement of thermodynamic properties [1]. Nowadays, however, there exist sensitive direct techniques to study magnetodynamics (both linear and nonlinear processes) involving spin-wave excitations. Spin waves are excited using the following techniques: via an rf Oersted field produced by various kinds of antennas [16], by light scattering (ultrafast laser pulses) [17], by neutron scattering [4], through parametric amplification of SWs from thermal fluctuations [9], via magnetoelectric interactions [18], and by spin transfer torque (STT) [19].

1.2 Coupling between two ferromagnet layers in trilayer spin valves

1.2.1 Main contributions to the magnetic Hamiltonian

The energy of the magnetic system can be mainly expressed by the exchange energy and the magnetic dipole–dipole energy and, in the case of an anisotropic system, anisotropy energy. These three terms are expressed respectively as:

$$\mathcal{E}_{ex} = \sum_{<i,j>} J_{i,j} S_i . S_j \tag{1.14}$$

$$\mathcal{E}_d = (g\mu_B)^2 \sum_{<i,j>} \left(\frac{S_i . S_j}{r_{i,j}^3} \frac{3(S_i . r_{i,j})(S_j . r_{i,j})}{r_{i,j}^5} \right) \tag{1.15}$$

$$\mathcal{E}_a = \sum_{<i>} K (S_i^Z)^2. \tag{1.16}$$

The exchange interaction is a short-range interaction, and in most cases it is sufficient to consider only nearest neighbor sites. Equation 1.13 shows the simplest form of the exchange energy. Equation 1.14 shows the dipole–dipole interaction contribution to magnetic energy. There is a magnetic moment $g\mu_B S_i$ corresponding to each spin S_i. The dipole–dipole interaction is much smaller than the exchange interaction (2–3 orders of magnitude smaller). However, for the magnetic dynamic properties (e.g., spin waves) at small enough wavenumbers (long wavelengths), the effect of the dipole–dipole interaction becomes significant, as the dipole–dipole interaction is long range and the exchange interaction is short range.

There are other contributions to the Hamiltonian of a magnetic system, including anisotropy. Anisotropy arises from the interaction of the magnetic moment of atoms with the electric field of the crystal lattice. Equation 1.15 shows a simplified description of the anisotropy contribution in a uniaxial (noncubic) ferromagnet, where K is an anisotropy constant [5].

1.2.2 Interlayer exchange coupling (IEC)

Trilayer FM/NM/FM systems have been the subject of many studies due to their applications in magnetic recording devices and nonvolatile magnetic random memories [20]. Variation of the intervening nonmagnetic interlayer tunes not only the strength of coupling, but also the type of coupling for ultrathin interlayer thicknesses. Bilinear coupling is one of strong models that fits the resonance condition of such systems. This coupling is described as bilinear, since the relative surface coupling energy is proportional to the magnetization product:

$$E_c = -J m_i m_{i+1}. \tag{1.17}$$

Generally, bilinear coupling in spin-valve structures or MTJs results from the combination of two contributions [21]:

RKKY interaction

The conduction-electron-mediated exchange coupling, which oscillates in sign as a function of the thickness of the metallic spacer layer and which is closely related to the well-known RKKY interaction [22] between magnetic impurities in a nonmagnetic host. This coupling was first observed in 1986 [23].

Néel coupling

Dipolar magnetic coupling (also known as Néel coupling or 'orange-peel' coupling) is ferromagnetic and arises from magnetostatic charges present at the interfaces and induced by surface roughness. This model predicts an exponential increase in dipole coupling between the magnetic layers with decreasing spacer thickness (Fig. 1.4).

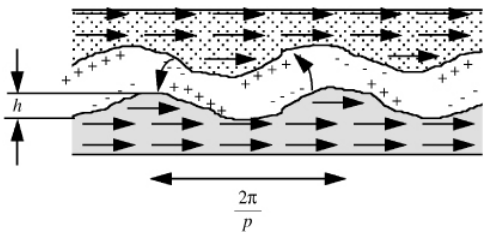

Figure 1.4: Schematic representation of a trilayer with conformal sinusoidal interface roughness inducing orange-peel FM coupling [21].

1.2.3 Spin pumping

While the static IEC is oscillating and short-ranged in nature, there also exists a dynamic and long-ranged coupling between magnetic layers, called spin pumping. The concept of spin pumping describes how the leakage of angular momentum (spin current) from a precessing magnetic film may be absorbed at the interface to another magnetic/nonmagnetic layer, which provides an additional damping term [24, 25, 26]. The dimensionless damping coefficient is then given by $\alpha = \alpha_{(0)} + \alpha_{\mathrm{sp}}$, where $\alpha_{(0)}$ is the intrinsic damping of the precessing layer and α_{sp} is the spin-pumping-induced term.

1.2.4 Models for fitting FMR modes of a trilayer system

The Kittel equation is well defined and widely used due to its simplicity, though it can only be used for single layers. In the case of multilayer systems, one approach is to consider each resonance mode individually and to use the Kittel equation by adding an exchange

field H_{add} [27, 28] to the internal field due to coupling. However, we observed that this method not only gave quite poor fits, but the J' values determined independently from $H_{\text{add}}^{\text{Py}}$ and $H_{\text{add}}^{\text{Co}}$ also differed significantly.

Improvements can be made if the heterogeneous nature of the structure is accounted for, instead of focusing on one component at a time. For this purpose, complex numerical models are suggested to obtain the eigenmodes of the multilayer system. One of these models is an approach where the relation between f_{r} and H_{r} is derived from the free energy of the system, giving the following expression [29, 30, 31]:

$$a\omega^4 + c\omega^2 + e\omega = 0 \tag{1.18}$$

where $\omega = 2\pi f_{\text{r}}$, and the coefficients a, c, and e contain the interlayer coupling, the magnetic properties, as well as the thickness of the magnetic layers.

Another model was suggested by Franco et al. in 2016 [32]. This was a simple model for the FMR of an exchange-interacting heterogeneous multilayer system that accounts simultaneously for all the resonance modes of the structure. Here we simplify the model for the trilayer structure (two FM layers), ignoring uniaxial anisotropy and cubic anisotropy due to the amorphous nature of both layers.

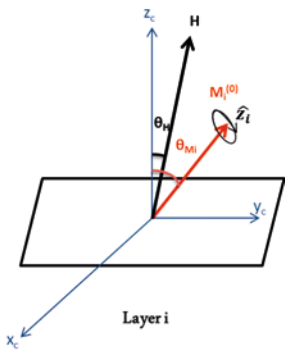

Figure 1.5: Cartesian coordinate system and notations for layer i [32].

Assuming that $\hat{z}_i$ lies in the equilibrium direction of M_i, the magnetization can be written in the form of a static term ($M_i^{(0)}$) and the dynamic magnetization as m_i, perpendicular to that. $i\omega_{res}/\gamma$, where $\omega_{res} = 2\pi f_{res}$ and γ is the gyromagnetic ratio, is given by the eigenvalues of the 4×4 dynamic matrix D_m:

$$D_m = \mu_0 \begin{pmatrix} -H_{y_0,x_0} & -H_{y_0,y_0} & -H_{y_0,x_1} & -H_{y_0,y_1} \\ H_{x_0,x_0} & H_{x_0,y_0} & H_{x_0,x_1} & H_{x_0,y_1} \\ -H_{y_1,x_0} & -H_{y_1,y_0} & -H_{y_1,x_1} & -H_{y_1,y_1} \\ H_{x_1,x_0} & H_{x_1,y_0} & H_{x_1,x_1} & H_{x_1,y_1} \end{pmatrix}. \tag{1.19}$$

The components $H_{\alpha_i\beta_\eta}$ of D_m are the dynamic fields linked to the second-order combinations of the dynamic components of the magnetizations. The internal dynamic fields for each individual layer are given by:

$$\begin{aligned} H^I_{x_ix_i} &= HC_S(M_i,H) - M^i_s(\cos^2\theta_{M_i} - \sin^2\theta_{M_i}) \\ H^I_{y_iy_i} &= HC_S(M_i,H) - M^i_s\cos^2\theta_{M_i}, \end{aligned} \tag{1.20}$$

where $C_S(A,B) \equiv \cos\theta_A\cos\theta_B + \sin\theta_A\sin\theta_B$, and $\theta_{A(B)}$ is the angle that the vector $A(B)$ forms with the normal of the layer z_c. The first term in both equations stems from the Zeeman energy, and the second term from the demagnetization field. H is the magnitude of the applied field and M^i_s is the saturation magnetization of layer i. To account for the interlayer exchange coupling, the following fields need to be included:

$$\begin{aligned} H^J_{x_ix_i} = H^J_{y_iy_i} &= \frac{J_{eff}}{\mu_0 M^i_s t_i} C_S(M_i,M_j) \\ H^J_{x_ix_j} &= -\frac{J_{eff}}{\mu_0 M^j_s t_i} S_C(M_i,M_j) \\ H^J_{y_iy_j} &= -\frac{J_{eff}}{\mu_0 M^j_s t_i}, \end{aligned} \tag{1.21}$$

where $S_C(M_i,M_j) \equiv \sin\theta_{M_i}\sin\theta_{M_j} + \cos\theta_{M_i}\cos\theta_{M_j}$, and t_i is the thickness of layer i. J_{eff} is the exchange interaction between FM layers and is positive for FM EC. The dynamic fields that compose the matrix D_m are calculated by adding the internal fields (1.15) and interlayer EC contributions (1.16) for each layer, as given by

$$H_{\alpha_i\beta_\eta} = H^I_{\alpha_i\beta_\eta} + H^J_{\alpha_i\beta_\eta}, \tag{1.22}$$

where α and β are any contribution of x, y, and η is either i or j. The susceptibility tensor can be obtained by using:

$$\chi = D_g^{-1} M_T, \tag{1.23}$$

where

$$M_T \equiv \begin{pmatrix} 0 & -M^0_s & 0 \\ M^0_s & 0 & -M^1_s \\ 0 & M^1_s & 0 \end{pmatrix}$$

and the matrix D_g is given by: $D_g = i\frac{\omega}{\gamma}W + D_m$. ω is the angular frequency of the microwave field, and the matrix W is given by:

$$W = \begin{pmatrix} 1 & g_0 & 0 \\ -g_0 & 1 & g_1 \\ 0 & -g_1 & 0 \end{pmatrix},$$

with g_i the Gilbert damping parameter of layer i.

By having dynamic susceptibility, the FMR resonance linewidth can be extracted by numerically solving:

$$\mathrm{Im}[\chi_{yy}(\omega, H^{\omega}_{res} + \Delta H^{\omega}_{lw})] = \frac{1}{2}\mathrm{Im}[\chi_{yy}(\omega, H^{\omega}_{res})], \tag{1.24}$$

where $\mu_0 \Delta H^{\omega}_{lw}$ is the field linewidth of the oscillation mode related to the resonance field $\mu_0 H^{\omega}_{res}$ and the frequency ω.

1.2.5 Anticrossing at the resonance coincidence point in collective regime

Exchange coupled magnetic layers exhibit collective dynamics and their ferromagnetic resonance (FMR) spectra display two modes – acoustical and optical – corresponding to in-phase and out-of-phase precession, respectively. The model of Franco et al. for the case of a perpendicular applied field in a CoFe/NiFe bilayer shows that the layers cross each other at field $\mu_0 H \approx 1.345T$ when $J_{eff} = 0$. By adding an FM EC at the interface, the model predicts a frequency gap of Δf_g at the crossing point (CP), Figure 1.6(a). The FM acoustic and optic modes at weak fields follow the NiFe and CoFe respectively. This is because, for weak applied fields, the resonance frequency of the NiFe is lower than that of CoFe. The opposite happens for strong fields after the CP. Thus, the modes switch their respective governing layers. It is at this transition from one governing layer to another that the gap appears. Figure 1.6 (b) shows the linewidth behavior of both acoustic and optic modes in the vicinity of the crossing point. It shows that the evolution of the linewidth is the same as the evolution of the frequency in Figure 1.6 (a). This confirms that the change in the governing layer strongly affects the frequency linewidth.

1.2.6 Fano resonance

Fano interference is a universal phenomenon, as the characteristics of the interference do not depend on the characteristics of the material. In spintronics, Fano resonance can be utilized in practice to implement quantum probes that provide important information on the geometric configuration and internal potential fields of low-dimensional structures [33]. Other potential applications of Fano resonance include new types of spintronics devices, such as Fano transistor [34] and Fano filters. In addition, from the basic science point of view, there are a few wave phenomena that represent milestones in modern physics—such as Young's interference in optics or Ahoronov–Bohm (AB) interference in quantum mechanics. Undoubtedly, Fano interference phenomena are of this type [33].

If the coupling parameter q becomes very strong ($q \gg 1$), then the Fano profile reduces to a symmetric Breit–Wigner (BW) (or Lorentzian) lineshape [35]. It has been shown that BW resonances arise due to the interference of two counterwaves in the same scattering channel. On the other hand, Fano resonance takes place due to wave interference in different channels.

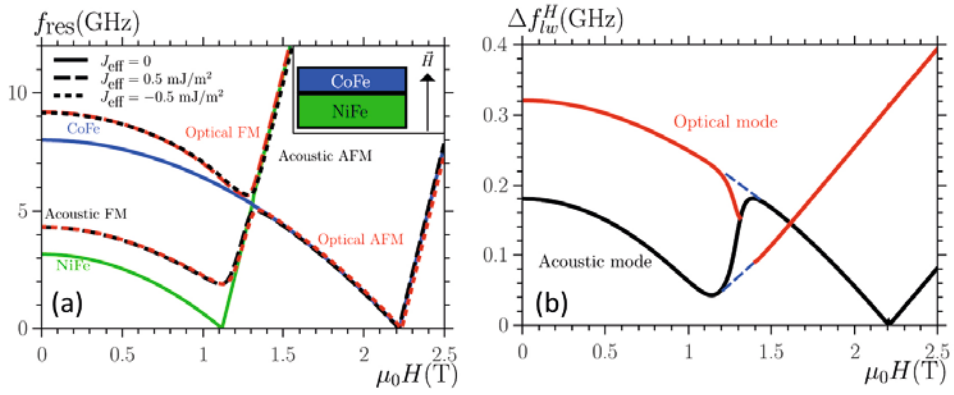

Figure 1.6: Theoretical model of resonance condition of exchange-coupled CoFe/NiFe bilayer in perpendicular field. (a) Frequency vs. field of the acoustic and optic modes for both positive and negative values of coupling (± 0.5 mJ/m^2), in comparison to the case where $J = 0$ mJ/m^2. (b) Linewidth vs. field of the acoustic and optical FM modes of a NiFe/CoFe bilayer ($J = +1$mJ/m^2) [32].

1.2.7 A classical analogy for Fano resonance: two coupled oscillators

Considering a pair of harmonic oscillators coupled by a weak spring, this section reviews the equation of motion for the behavior of the forced oscillator. For two harmonic oscillators with coupling υ_{12}, this can be written as:

$$\ddot{x}_1 + \gamma_1 \dot{x_1} + \omega_1^2 x_1 + \upsilon_{12} x_2 = a_1 e^{i\omega t} \tag{1.25}$$

$$\ddot{x}_2 + \gamma_2 \dot{x_2} + \upsilon_{12} x_2 = 0,$$

where $a_1 e^{i\omega t}$ is the external force. The eigenmodes of such a system can be written as:

$$\widetilde{\omega_1}^2 \approx \omega_1^2 - \frac{\upsilon_{12}^2}{\omega_2^2 - \omega_1^2}, \qquad \widetilde{\omega_2}^2 \approx \omega_2^2 + \frac{\upsilon_{12}^2}{\omega_2^2 - \omega_1^2}. \tag{1.26}$$

The steady-state solutions of this system are:

$$x_1 = c_1 e^{i\omega t}, \qquad x_2 = c_2 e^{i\omega t}, \tag{1.27}$$

where c_1 and c_2 are the amplitudes of the forced oscillator and the coupled oscillator is given by:

$$c_1 = \frac{(\omega_2^2 - \omega^2 + i\gamma_2\omega)}{(\omega_1^2 - \omega^2 + i\gamma_1\omega)(\omega_2^2 - \omega^2 + i\gamma_2\omega) - \upsilon_{12}^2} a_1$$

$$c_2 = -\frac{\upsilon_{12}}{(\omega_1^2 - \omega^2 + i\gamma_1\omega)(\omega_2^2 - \omega^2 + i\gamma_2\omega) - \upsilon_{12}^2} a_1. \tag{1.28}$$

The phases of the oscillations are defined by:

$$c_1(\omega) = |c_1(\omega)|e^{-i\phi_1(\omega)}$$

$$c_1(\omega) = |c_1(\omega)|e^{-i\phi_1(\omega)}. \tag{1.29}$$

The phase difference between the two oscillators is: $\phi_2 - \phi_1 = \pi - \theta$, where the extra phase shift $\theta = \arctan(\frac{\gamma_2\omega}{\omega_2^2 - \omega^2})$. The effective friction (γ_2) for normal modes causes the amplitude of the oscillators to be limited. The amplitude and phase of both oscillators as a function of the frequency of an external force are shown in Figure 1.7 [33].

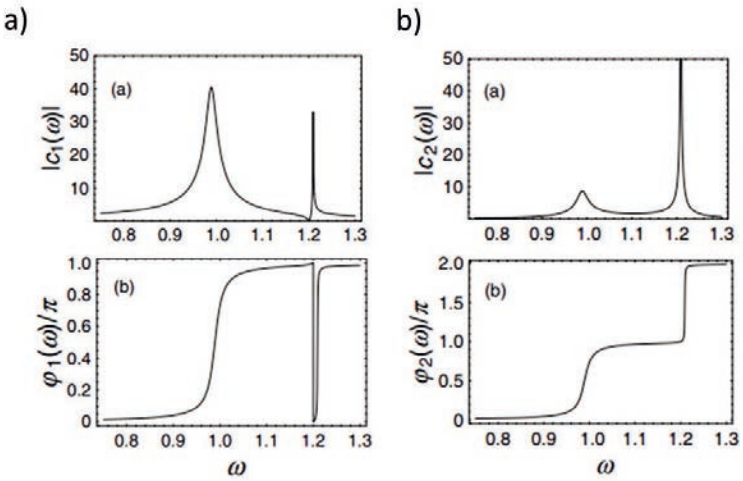

Figure 1.7: Resonance amplitude and phase of a forced oscillator (a) and a coupled oscillator (b) in a harmonic coupled system. The frequency is in the unit of natural frequency ω_1. The amplitude has two peaks near the eigenfrequencies. Here, $\gamma_1 = 0.025;\ \gamma_2 = 0;\ \upsilon_{12} = 0.1$ [33].

Chapter 2

Methods: fabrication and measurement

Nanocontacts (NC) on pseudo-spin-valves are particularly promising for high-frequency spin-torque oscillators (NC-STOs) [36, 37, 38, 39, 40, 41, 42, 43, 44, 45, 46, 47, 48, 49, 50, 51] and for the emerging field of ST-based magnonics, [52, 53, 9, 54, 55] (Section 4.3) where highly nonlinear auto-oscillatory modes are utilized for operation. I have performed fundamental research on this structure by using ferromagnetic resonance techniques (FMR and ST-FMR), as described in Chapters 3 and 4. In this chapter, I briefly go through the steps of device fabrication and then explain the ferromagnetic resonance techniques used for the measurement of blanket samples and nanocontact devices.

2.1 Device fabrication

The fabrication of NC-STOs has previously been developed in the Applied Spintronics group [43]. The stack of thin film layers is deposited by an AJA magnetron sputtering system on SiO_2/Si substrate pieces (Fig. 2.1(a)). The mesa (the active area) and alignment marks are then prepatterned by photolithography and the mesa is defined by ion milling using SIMS monitoring (Fig. 2.1(b)). Afterward, the process is followed by sputtering the insulating layer, SiO_2, on top of the sample (Fig. 2.1(c)). Then, by means of E-beam lithography (EBL), the nanogap is defined in the middle of the mesa flanked by two micron-size gaps, followed by SiO_2 reactive ion etching (RIE), (Fig. 2.1(d)). Finally, the fabrication of the NC-STO finished with the creation of electrical pads in a lift-off process (Fig. 2.1(e)). After finishing each step and before going on to the next, an optical/SEM inspection is performed to determine if the micro/nanofabrication process was clean.

Regarding the devices included in this thesis, the fabrication process is the same for the whole work and only the size of the nanocontact (see Section 3.1), the thickness of the bottom-layer electrode (Section 3.2), and the thickness of the spacer layer (Chapter 4) were altered for the different sections in this thesis.

Here, I briefly introduce the tools and parameters used in the fabrication process. Except for the blanket film process, all fabrication processes were carried out in the MC2 clean room at Chalmers University.

2.1.1 Sample deposition by magnetron sputtering

Physical vapor deposition (PVD) technologies are used to deposit the thin film onto a substrate from a vapor phase inside a vacuum chamber. One of the main techniques of this kind is sputtering. This involves ejecting atoms or molecules from a target using an ionized gas (usually an inert gas such as Ar) and condensing them onto the substrate. This can be done by means of an electrical voltage to create a plasma around the target. The advantage of this technique is the low temperature of the substrate, which makes it widely applicable in the integrated circuit industry for the deposition of semiconductors onto Si wafers. Another important advantage is that high melting point materials can easily be sputtered. The sputtering method has much a higher energy than the evaporation method, which means that the sputtered material is usually in the form of ions with the ability to generate very dense thin films on the substrate; the final significant advantage is that sputtering is much less sensitive to the target's stoichiometry than other methods of PVD, which makes it applicable to deposition of alloy materials such as NiFe and YIG.

One common way to enhance sputtering is to use what is known as a magnetron sputtering system. In magnetron sputtering, permanent magnets are located behind the target in order to spiral the free electrons in a magnetic field directly above the target surface. This prevents the free electrons, which are repelled by the negatively charged target, from bombarding the substrate, and as a result preventing overheating and structural damage; Also, the electrons travel a longer distance, increasing the probability of further ionizing Argon atoms.

In the present work, AJA ATC Orion-8 with seven guns from Applied Spintronics group was used. This system is a confocal sputtering system, with the multimagnetron sputtering sources coordinated specifically in a circular pattern and directed towards a common focal point. Using several different magnetron sources, it is possible to deposit structures consisting of several different layers of materials. Figure 2.1(a) shows the schematic of Pd/Cu/Co/Cu/NiFe/Cu/Pd multilayers that make up a pseudo-spin-valve structure sputtered on a thermally oxidized Si substrate, where NiFe ($Ni_{80}Fe_{20}$) and Co play the role of the free and fixed layers, respectively. For depositing a conductive material such as copper or palladium, it is possible to utilize either a rf or dc power supply, but for nonconductive materials such as SiO_2, a rf power supply is needed.

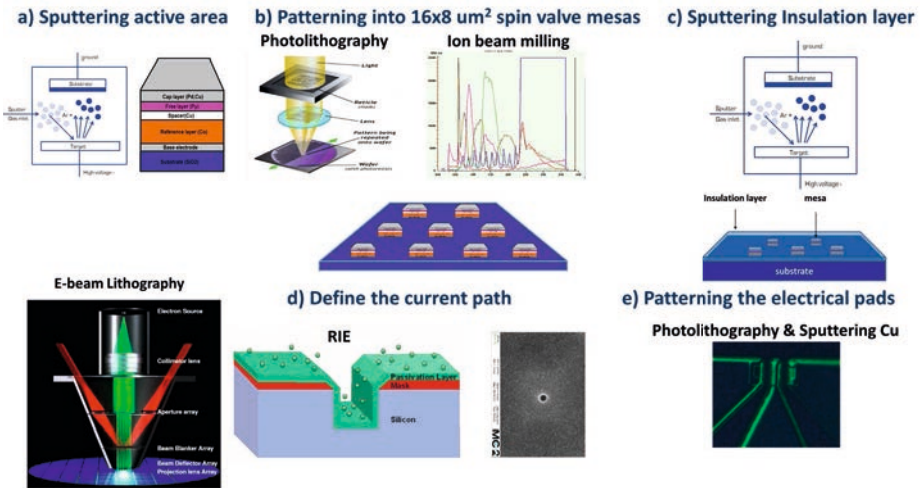

Figure 2.1: (a): Left: schematic of the sputtering method; right: multilayer stack processed by magnetron sputtering. (b) Left: Schematic of photolithography method; right: SIMS traces for the sample: Pd (3 nm) /Cu (15 nm) / Co (8 nm) / Cu (8 nm) / NiFe (4.5 nm)/ Cu (3 nm) / Pd (3 nm); bottom: mesa after ion milling and removal of resist. (c) Schematic of the sample covered by an insulation layer (SiO_2) through sputtering. (d): Left: schematic of e-beam lithography method; middle: schematic of RIE method (to remove SiO_2 from exposed areas); right: SEM image of nanogap processed with EBL and RIE; (e): optical image of electrical pads on top of the nanogap (signal pad), flanked by two micron size gaps (ground pads).

2.1.2 Mark alignment and prepatterning of mesa and electrical pads by photolithography

Photolithography (or UV lithography) is a process used in fabricating micron-sized parts of a thin film. In this method, UV light transfers a geometric pattern from a photomask to a

light-sensitive chemical "photoresist" on the substrate. We used this method to prepattern mark alignments and to define the borders of the mesas. The first photolithography step is simply aligned with the sample, as no previous pattern is present yet in the sample. Usually, in a multistep nano/microfabrication, the key point is the high-accuracy alignment of the micron and nanosized patterns in sequence. Thus, the first photo mask should include marks for the alignment of the next lithography level, in addition to the mesa pattern. Using a light field mask makes it easy to define bright field marks on the photo mask. Normally, two global marks are enough for each sample for both photo and e-beam lithography. The global marks are crosses 1 millimeter long and 15 microns wide. It should be noted that the marks should be located at the same x value, near the middle of the x-axis of the sample and near the borders of the y-axis of the pattern. Using this configuration of alignment marks, we can easily carry out alignment in the next photolithography level (the final step of prepatterning the electrical pads) by arranging the translational alignment with one alignment mark and the rotational alignment with the other. The parameters used in the first and last step of photolithography are listed in Tables 2.1 and 2.2, respectively.

First step: photolithography process parameters	
Resist	Shipley S1813
Spin speed	4000 rpm
Soft bake	2 min @ 115 C, hot plate
Exposure	contact mask, 5 sec
Development	1:30 min in MF319
Hard bake	30 min @ 120 C, oven

Table 2.1: Parameters of the first photolithography step for prepatterning the mark alignment and the mesa.

Last step: photolithography process parameters	
Resist 1	LOR 3A
Spin speed 1	1700 rpm
Soft bake 1	5 min @ 160 C, hot plate
Resist 2	Shipley S1813
Spin speed 2	4000 rpm
Soft bake 2	2 min @ 115 C, hot plate
Exposure	contact mask, 6.5 sec
Development	1:40 min in MF319

Table 2.2: Parameters used in the last photolithography step to prepattern the electrical pads.

2.1.3 Fabrication of mesas through ion beam milling

Ion milling is a physical dry-etching technique. In this method, a beam of ions (such as Ar) is used to sputter etch material exposed by the mask (typically a photoresist) to obtain the desired pattern. A 10° to 30° incident beam angle is much more efficient than normal (0°) incidence. In addition, by changing the beam angle to about 70° during the final seconds of the process, it is possible to remove the sidewalls created during etching. For accurate control during etching, the secondary ions coming from the material layers on the substrate surface can be analyzed. In this in situ technique, arrival at a specific underlayer can be determined. This "end-point" detection technique is called SIMS (secondary ion mass spectroscopy). As the milling process starts to penetrate the Cu bottom layer and into the SiO_2, the intensity of Cu starts to diminish, and the presence of SiO_2 is first detected and begins to increase significantly. Finally, the Cu intensity has reached a minimal value and the SiO_2 intensity is substantial. The advantage of ion milling to chemical methods is that it allows all known materials to be etched. In this project, an Oxford Ionfab 300 Plus at MC2 clean room at Chalmers was used. The parameters are listed in Table 2.3.

Ion milling process parameters	
V_{beam}	500 V
V_{acc}	300 V
I_{beam}	30 mA
Ar flow	8 sccm
rotation	10/min
Tilt	10° + 70° when reaching bottom Cu layer
resist removal	10 min in mr-Rem 400 remover (50 C), 3 min ultrasonic

Table 2.3: Parameters used in the process of ion milling to define the mesa.

2.1.4 Prepattern nanogap by E-beam lithography

Electron beam lithography (EBL) is one of the most important techniques in nanofabrication. The working principle is very similar to the photolithography. A focused beam of electrons is scanned across a sample covered by an electron-sensitive material (e-beam resist) that changes its solubility properties according to the energy deposited by the electron beam. Exposed areas are removed by developing process. The e-beam resist used in our work was ZEP resist, which is a positive EBL resist. The parameters are listed in Table 2.4.

Ion milling process parameters	
Resist	ZEP
Spin speed	4000 rpm
Soft bake	5 min @ 160 C, hotplate
Exposure	EBL
Development	2:00 min in n-amylacetate

Table 2.4: The parameters used in the e-beam lithography process to prepattern the nanogap-flanked two-micron gaps.

2.1.5 Etching of exposed e-beam resist areas through reactive ion etching

Reactive ion etching (RIE) is a dry-chemical etching technology. During RIE etching, low-pressure plasma containing high-energy ions and radicals interacts with openings at the surface of the sample covered with resist and forms unstable compounds. Various types of materials can be etched using RIE etching technology by optimizing etch parameters such as pressure, gas flow, and rf power. The recipe in this work used for removing the material inside the resist opening of SiO_2 is listed in Table 2.5.

Reactive ion etch process parameters	
gas flows	5 sccm CF_4, 20 sccm CHF_3, 30 sccm Ar
pressure	20 mTorr
rf power	100 W
V_{bias}	312 V
etch time	2:30 min
resist removal	oxygen plasma
resist removal	hot mr-remover 400 @ 55 C, heat bath 20 min, 5 min ultrasonic

Table 2.5: Parameters used in the process of reactive ion etching to etch through the openings after e-beam exposure.

2.2 Characterization of the trilayer stack and NC-STOs

2.2.1 Giant magnetic resistance

Magnetoresistance (MR), the change in electrical resistance of magnetic materials in response to an applied magnetic field, is a well-known phenomenon. It is dependent on the strength of the applied field and its relative orientation to the current; the magnitude of this effect for "anisotropic" magnetoresistant materials is reported to be about 2% at room

temperature. In 1988, Albert Fert and Peter Grünberg discovered another type of magnetoresistance in a trilayer structure (a spin valve), an order of magnitude higher (about 50% at low temperature [56]) than other magnetoresistive effects [56]; this is called "giant magnetoresistance" (GMR). In contrast to the AMR effect, GMR depends on the relative orientation of the magnetization in the layers, and not on the direction of the current. The simple explanation for this phenomena is based on the spin-dependent scattering process of spin-polarized electrons. If both FM layers in the spin valve structure have the same orientation of magnetization, the resistance of the device ($R\uparrow\uparrow$) reaches a minimum value; if the orientation of magnetization in both layers is opposite ($R\uparrow\downarrow$), the resistance of the device takes on its maximum value; in between these two extremes, the resistance is proportional to $\cos(\theta)$, where θ is the relative angle of the adjacent FM layers (Fig. 2.2). Since its discovery, academic and industrial laboratories have devoted much effort to investigating GMR because of the deep fundamental physics that controls this phenomenon and its enormous technological potential for the magnetic recording, storage, and sensor industries. In 2007, Albert Fert and Peter Grünberg were awarded the Nobel Prize in Physics for their discovery of GMR.

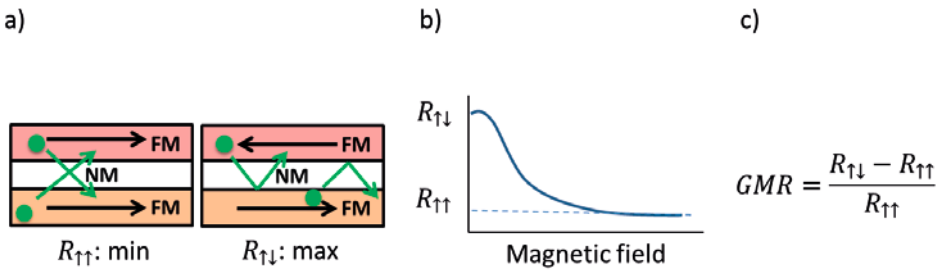

Figure 2.2: Schematic demonstrating the physical origin of the GMR effect. (a) Trilayer spin valve in minimum and maximum magnetoresistance configuration. The green circles and arrows show spin-polarized electrons in the local magnetization and their freedom to movement (their mean free path), respectively. (b) Variation of magnetoresistance as the magnetic field is swept. (c) The formula for calculating GMR.

2.2.2 Ferromagnetic resonance technique

Ferromagnetic resonance (FMR) is an experimental technique that allows the characterization and study of fundamental properties of different kinds of magnetic structures and multilayers [57, 58, 28]. Here I briefly review the basic physics behind it.

The Landau–Lifshitz–Gilbert differential equation predicts the rotation of the magnetization in response to torques [59]:

$$\frac{dM}{dt} = -\gamma M \times H_{eff} + \frac{\alpha}{M} M \times \frac{\partial M}{\partial t}, \tag{2.1}$$

where γ is the electron gyromagnetic ratio (being a characteristic of the collective motion of magnetic moments); this should not equal its value in a free state, and must be regarded as a parameter found by experiment. By applying asymptotic analysis to the data, NIST has reported $\frac{\gamma}{2\pi} = 29.5 \pm 0.05$ GHz/T for NiFe thin films. α is a dimensionless constant called the damping factor that describes a viscous-like loss proportional to the velocity of magnetization. The effective field H_{eff} is a combination of the external magnetic field, the demagnetizing field (magnetic field due to the magnetization), and certain quantum mechanical effects. This equation is valid strictly for uniform magnetization and the slow oscillation of M in space [7].

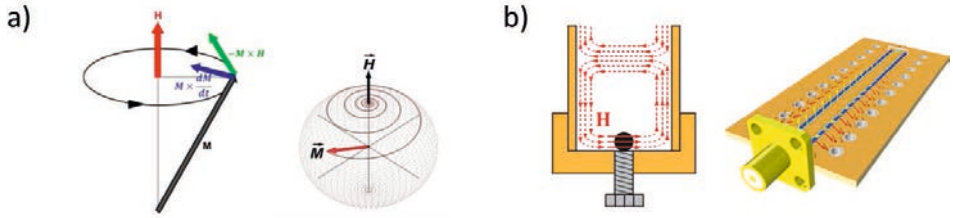

Figure 2.3: (a) Magnetization precession for motion with damping. (b) Schematic of cavity FMR used for bulk materials and coplanar wave guide used for thin films.

Considering the oscillation of magnetization under the influence of a given internal ac magnetic field,

$$H = H_0 + h_{\sim}, \qquad M = M_0 + m_{\sim}.$$

Polder was the first to present a solution of the equation of motion under steady and linearized conditions [60], and this leads to

$$m_{\sim} = \overline{\chi}.h_{\perp}, \tag{2.2}$$

where H_0 is static internal magnetic field and $\vec{h_{\perp}}$ is the transverse ac field regarding magnetization ($\vec{m}$). $[\chi]$ is the magnetic susceptibility tensor. From Equation 1.3, it can be seen that the nonzero components of the magnetic tensor approach infinity when ω approaches ω_H. This phenomenon is known as *ferromagnetic resonance*. Arkadyev predicted this phenomenon using a classical model as early as 1912, prior to the discovery of the electron's spin [61]. However, after the discovery of the nature of ferromagnetism in 1928 and the first theory of ferromagnetic resonance, proposed by Landau and Lifshitz in 1935 [59], ferromagnetic resonance was discovered experimentally by Griffiths in 1946 [62]

and explained theoretically by Kittel in 1948 [63]. This theory is widely used due to its simplicity.

The principal result of the theory is that the resonant frequency of a film is given by

$$\omega_0 = \gamma(B\mu_0 H_0)^{\frac{1}{2}} \tag{2.3}$$

where B is the magnetic induction in the specimen and $\mu_0 H_0$ is the strength of the internal magnetic field; Under the parallel applied field, B is given by

$$B = \mu_0 H_0 + \mu_0 M_s,$$

where μ_0 is the permeability of free space,M_s is the saturation magnetization of the ferromagnet [63], and $\mu_0 H_0$ is equal to

$$\mu_0 H_0 = \mu_0 H_{appl} + \mu_0 H_{add}$$

where $\mu_0 H_{\text{appl}}$ is the (applied) resonance field, and $\mu_0 H_{\text{add}}$ is the sum of additional in-plane fields, mainly represented by the anisotropy.

By fitting Equation 2.3 to the experimental data (ω_0, $\mu_0 H_{appl}$), the intrinsic parameters of FM materials (γ, M_s) can be extracted.

In the general case, when the applied field has an arbitrary angle (Fig. 2.4), this substitution can be used in the resonance equation of a thin film, Equation 2.3[64]:

$$B = \mu_0 H_0 + \mu_0 M_s \cos^2(\theta_{int}), \tag{2.4}$$

where θ_{int} is the internal field polar angle. Applying Ampere's law and Gauss' law for magnetism to the boundary of the thin film results in Equation 2.5:

$$\mu_0 H_{appl} \cos(\theta_{appl}) = \mu_0 H_0 \cos(\theta_{int}) \tag{2.5}$$

$$\mu_0 H_{appl} \sin(\theta_{appl}) = (\mu_0 H_0 + \mu_0 M_s) \sin(\theta_{int}).$$

Assuming γ and M_s are known parameters, by calculating Equations 2.3, 2.4, and 2.5, the behavior of the resonance frequency (ω_0) versus the applied field (H_{appl}) for oblique magnetized thin film can be extracted analytically.

I used NanOsc's broadband (2–40 GHz) PhaseFMR spectrometer to apply microwave fields to the sample via a coplanar waveguide (CPW) and employed a lock-in technique for signal detection. A schematic of the experimental setup is shown in Figure 2.5. The f–H resonance condition is extracted with a Lorentzian fit [65, 66] (Eq. 2.6) to the FMR derivative signals.

$$f = \text{offset} + k\frac{\left(\Delta H^2 - 4(H - H_r)^2\right) sin(\epsilon)}{\left(\Delta H^2 + 4(H - H_r)^2\right)^2} + k\frac{-8(H - H_r)\Delta H cos(\epsilon)}{\left(\Delta H^2 + 4(H - H_r)^2\right)^2}, \tag{2.6}$$

where H and H_r are applied and resonance fields, respectively, and ΔH is the linewidth of the corresponding peak. $\frac{k}{\Delta H}$ is amplitude and ϵ is the phase of the signal.

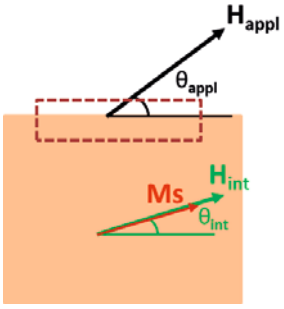

Figure 2.4: Schematic of magnetic configuration of FM material inside an oblique magnetic field. The Ampere's law/Gauss' law integral is evaluated on the dashed closed line/surface. The integrals on the left and right borders cancel each other. The integral on the top and bottom line/surface yields Equation 2.5.

Damping can be extracted from the linear dependence (Eq. 2.7).

$$\mu_0 \Delta H = \mu_0 \Delta H_0 + \frac{4\pi}{\gamma} \alpha f_{res}. \tag{2.7}$$

Figure 2.3(b) shows a schematic of an FMR cavity, in which an alternating field excites magnetodynamics in the bulk sample and a schematic of the coplanar waveguide (CPW) in which the rf Oersted field drives the magnetodynamics in thin films.

2.2.3 Spin-torque ferromagnetic resonance technique

In the previous subsection, I mentioned two widely used FMR techniques for measuring the magnetodynamics of bulk materials and thin films. However, conventional FMR techniques lack the sensitivity to measure magnetodynamics in the nanoscale devices of interest in the study of fundamental physics and in broadband technical applications to MRAM memory [67, 68] and data storage devices [69]. Here, we introduce spin-torque-driven ferromagnetic resonance technique to the measurement of sub-100-nm-scale devices.

Unlike more conventional FMR measurement techniques, where a resonant cavity or waveguide is used to generate rf magnetic excitation fields, the resonant precession in an ST-FMR measurement is assumed to be primarily a result of the spin torque from a spin-polarized current. This effect can excite oscillations or flip the orientation of the magnetization. Spin torque ferromagnetic resonance (ST-FMR) [70, 71, 69, 72, 73, 74, 75, 76, 77] is a powerful and versatile tool that enables the characterization of magnetodynamics on the nanoscale. The method involves injecting a rf current into a laterally confined giant magnetic resistance (GMR) or magnetic tunnel junction device, driving one of the magnetic layers into resonance. Figure 2.6 shows the basic physics of the ST-FMR technique. Figure 2.6(a) represents the positive half-period of the unpolarized rf current entering the

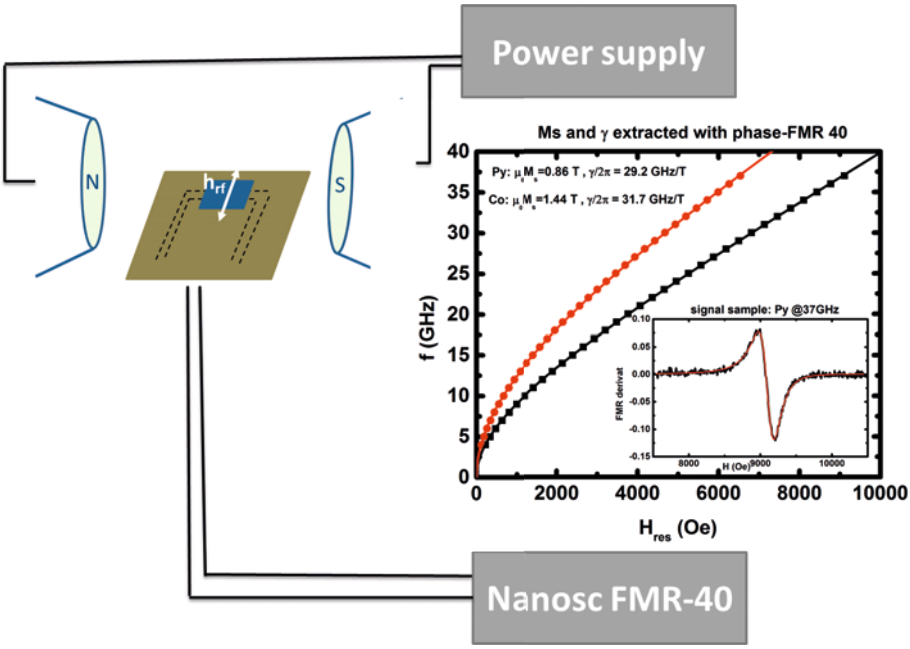

Figure 2.5: Schematic of FMR setup: The graph shows typical FMR measurement data and analysis. The f–H resonance data points are extracted by fitting a Lorentzian to the signals.

reference layer; it is then polarized to the orientation of the reference layer magnetization and finally, by passing through the free layer, exerts a negative torque on the local magnetization. Figure 2.6(b) represents the negative half-period of the rf current entering the free layer, being polarized by passing through it and then, at the interface of the reference layer, the electrons with opposite orientation of spins to the local magnetization reflect and pass back through the free layer. Finally, the spin current flowing back exerts a positive torque on the local magnetization of the free layer, as shown in the diagram. Figure 2.6(c) shows the ΔR of a period of rf current that results from variation in the magnetic resistance of the sample due to GMR effect (as explained in the previous section). Homodyne mixing of the rf current and device resistance oscillations results in a voltage across the device that can be measured by extracting its DC component with the lock-in technique.

However, we will see in the next chapter that, although the ST-FMR technique is used to excite the magnetodynamics in our system, the ST cannot be responsible for the excitation. Chapter 3 is devoted to determining the basic physics of the magnetic dynamic excitation in the in-plane magnetized nanocontact trilayer pseudo-spin-valve. In Section 4.3, I use the ST-FMR technique to excite and detect magnetodynamics in coupled nanocontact trilayer pseudo-spin-valve in an oblique field.

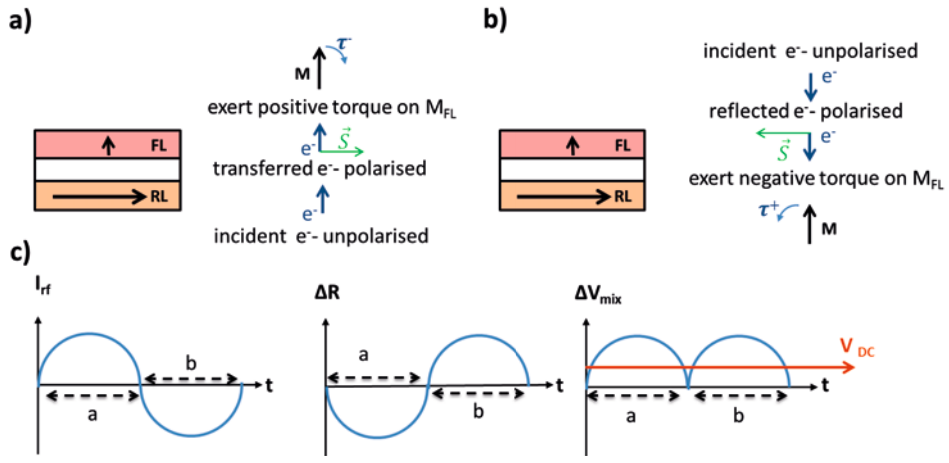

Figure 2.6: (a) The positive half-period of the rf current passing through the trilayer spin valve, exerting a negative torque on the local magnetization of the free layer. (b) The negative half-period of the rf current passing through the trilayer spin valve, exerting a positive torque on the local magnetization of the free layer. (c) The plot of one period of rf current, with alternative magnetoresistance due to the GMR effect, resulting in mixing voltage across the device. V_{DC} is extracted by the lock-in technique.

Figure 2.7 (a) and (b) show respectively the schematic and experimental setups of the ST-FMR circuit. All measurements were performed at room temperature in a custom-built probe station utilizing a uniform magnetic field. Both a microwave generator and a lock-in amplifier (which were connected to the device using a bias-tee) were utilized to perform FMR measurement. The rf power injected into the NC was fixed in Chapter 3 and set to -14 dBm in Section 3.1 and -10 dBm in Section 3.2, which ensures that the excited magnetodynamics is in the linear regime. The resulting dc mixing voltage [69], V_{mix}, was measured as a function of the magnetic field and at a fixed excitation frequency. The microwave current was amplitude modulated at a low (98.76 Hz) modulation frequency for lock-in detection of V_{mix}.

Equation (2.6) is a derivative Lorentzian and is used for fit of FMR measurements. However, for fitting to the ST-FMR spectra, we use:

$$f = \text{offset} + \sum_{i=\text{FMR,SWR}} k\left[\frac{\Delta H^{i^2} cos(\epsilon)}{\Delta H^{i^2} + 4\left(H - H_{\text{r}}^{i}\right)^2} + \frac{\Delta H^{i}(H - H_{\text{r}}^{i}) sin(\epsilon)}{\Delta H^{i^2} + 4\left(H - H_{\text{r}}^{i}\right)^2}\right], \tag{2.8}$$

where H and H_{r}^{i} are the applied and resonance fields, respectively, and ΔH^{i} is the linewidth of the corresponding peak. $\frac{k}{\Delta H^{i}}$ is amplitude and ϵ is the phase of the signal.

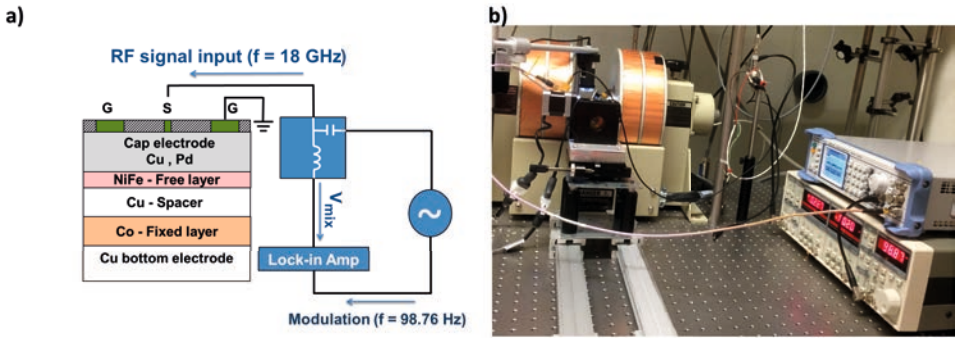

Figure 2.7: (a) Schematic of ST-FMR circuit and the nanocontact pseudo-spin-valve. (b) Experimental setup for all measurements in the next chapter.

Chapter 3

Spin waves in in-plane magnetized NC-STOs

Though ST-FMR studies of magnetic tunnel junction (MTJ) devices and all-metallic spin-valve nanopillar devices have dominated the literature [71, 69, 72, 73, 74], there has been an increasing number of studies utilizing point-contact and nanocontact (NC) devices on extended multilayer film stacks [75, 78, 79, 80, 81].

In this chapter, which is based on two manuscripts, I describe the utilization of the ST-FMR technique to excite and detect spin-wave resonance (SWR) spectra in tangentially magnetized NCs. The nature of the spin waves is determined by the analytical approach and numerical simulation. The origin of the magnetodynamics of detected spectra is then explored by numerical simulation. Afterward, I study tuning the spin wave spectra using lateral current spread. To this end, different thicknesses of the Cu bottom layer are used to control the lateral current spread.

3.1 Homodyne-detected ferromagnetic resonance of in-plane magnetized nanocontacts

3.1.1 The peak asymmetry in ST-FMR spectra of Py in the NC-geometry literature

In the NC geometry literature [75, 78, 79, 80, 81, 82], the observed ST-FMR spectra of the NiFe-based free layers have been analyzed as a single resonance, despite the significant peak asymmetry that hints at additional contributions. The linewidth of this asymmetric peak has not been understood so far [75]. The same study also notes that the typical field condition of an in-plane field aligning both magnetic layers in parallel should not result in any ST, calling into question the fundamental excitation mechanism of the observed spectra. This significant discrepancy has been tentatively explained as being caused by local misalignments due to sample imperfections. However, given how robust ST-FMR measurements are over sets of different devices, it is rather unsatisfactory to have to refer to unknown extrinsic factors for the ST-FMR technique to function. It appears that the rf Oersted field generated by the microwave current injected into the NC could be at play here [81]. Both a better fundamental understanding of the linear spin wave (SW) modes in the NC geometry and of their excitation mechanism are highly desirable.

3.1.2 Study of ST-FMR spectra of Py with different NC diameters

The fabrication process of NC on top of pSV (Co / Cu (8 nm) / NiFe) is explained in Chapter 2. The circular NCs have nominal diameters D of 90 nm, 160 nm, and 240 nm.

All measurements were performed utilizing a uniform *in-plane* magnetic field. The measurement setup is shown in Figure 2.7. The rf power injected into the NC is -14 dBm, which ensures that the excited magnetodynamics is in the linear regime.

3.1.3 Fit the Py spectra with two Lorentzian functions

The field-swept spectra measured for different frequencies, vertically offset for clarity, are shown in Figure 3.1 (inset) for the $D = 160$ nm sample. As shown in the main panel of Figure 3.1, the dominant resonance peak (points) can be well fit (solid line) with the Kittel equation, which results in $\mu_0 M_s = 0.85 \pm 0.02$ T and a negligible magnetocrystalline anisotropy.

Interestingly, it becomes clear upon closer inspection that the measured spectra are highly asymmetric, exhibiting a significant shoulder on the low-field side of the dominant resonance peak. In Figure 3.2, we show a single representative resonance at $f = 18$ GHz for the $D = 160$ nm sample. While it is well-known that the mixing voltage can be intrinsically asymmetric [83, 71, 84], it is important to point out that we cannot fit our data with a single resonance having both symmetric and antisymmetric contributions. Most importantly, the prior theoretical results are virtually independent of the NC diameter, in

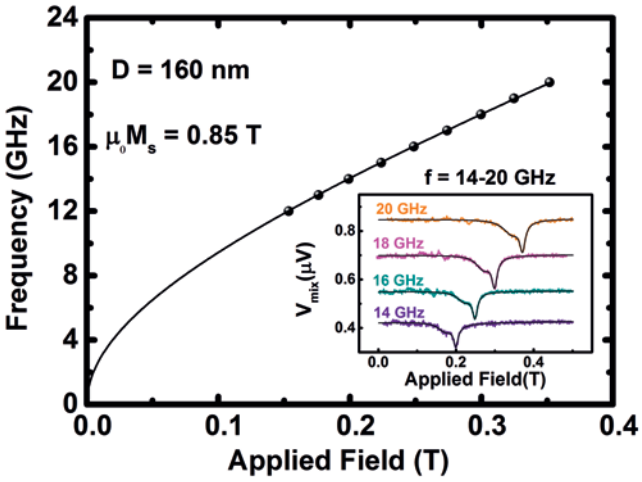

Figure 3.1: Inset: ST-FMR spectra at four different frequencies for the $D = 160$ nm sample. Main figure: Plot of the field position of the dominant resonance peak. The resonance fields can be well fit by the Kittel equation using $\mu_0 M_s = 0.85 \pm 0.02$ T for the NiFe layer.

direct contrast to our experimental observations. In order to properly fit (red solid line) the entire spectrum, we must instead use *two* Lorentzian functions, each with its own resonance field and linewidth, as shown in Figure 3.2 (inset). The fit (equation (2.8)) shows a vanishing antisymmetric contribution to the lineshape for each of the resonances.

As the frequency versus field behavior of the main resonance mode can be fit well with the Kittel equation, Figure 3.1, we ascribe this peak to the FMR mode of the NiFe layer and the second low field mode with a higher-order spin wave resonance (SWR), which will be discussed in detail later.

The linewidth versus frequency behavior of both the FMR and SWR modes are plotted in Figure 3.3 for three different NC diameters. Three different significant observations can be made. First, the FMR mode shows a clear linear increase in linewidth with the frequency, from which the Gilbert damping α can be extracted using Equation (2.7).

Our measured values of α, which are all on the order of 0.01, are also consistent with those measured in Ref. [85]. This provides further evidence that the dominant resonance mode can indeed be correlated with the usual FMR mode of NiFe. Second, the linewidth of the SWR mode is mostly independent of frequency, indicating that the primary origin of the linewidth is not damping. Third, the inhomogeneous broadening is approximately *inversely proportional* to the NC diameter, which at first seems counterintuitive, as one would expect a larger NC to sample a larger sample volume and therefore include more inhomogeneities. The origin of this interesting effect will be explained later.

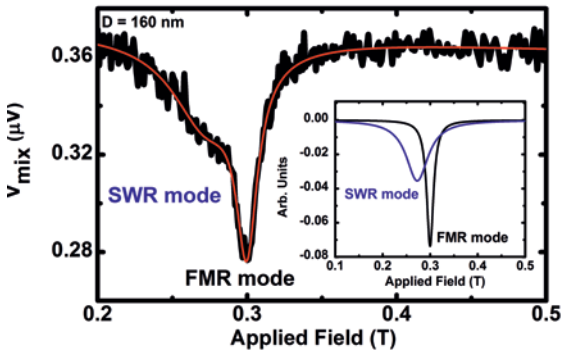

Figure 3.2: Zoom-in of a representative ST-FMR spectrum of the $D = 160$ nm sample taken at $f = 18$ GHz and $I_{rf} = 1.3$ mA, together with a fit (the red line) based on two Lorentzians, as described in the text. The inset shows the two individual contributions of the quasiuniform FMR mode (black) and the spin wave resonance (blue).

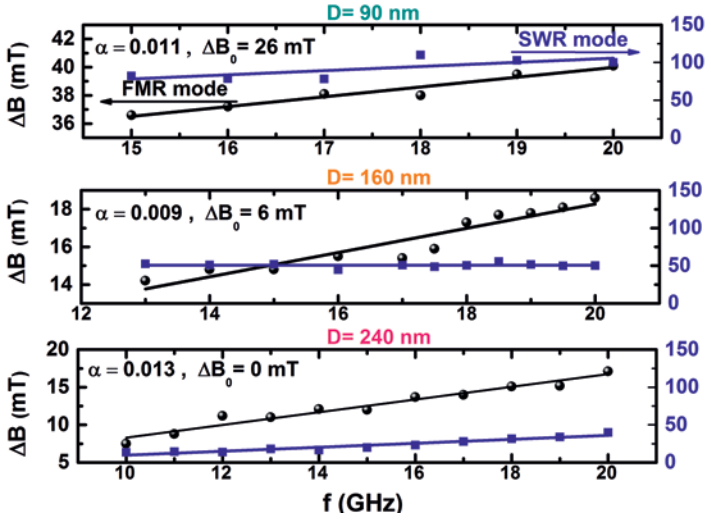

Figure 3.3: The measured (dots) and fitted (solid lines) linewidths of the FMR and SWR modes are shown for the different NC diameters.

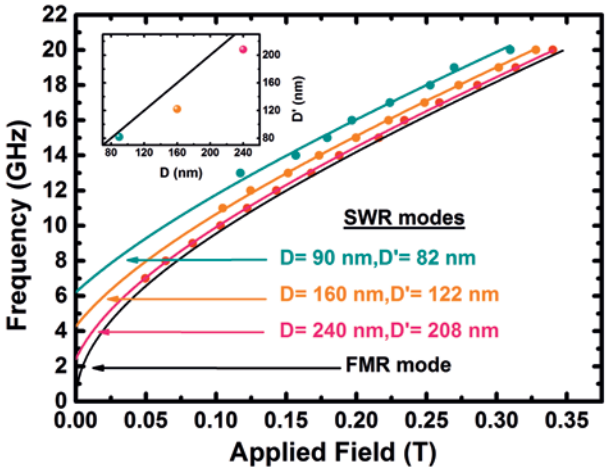

Figure 3.4: Measured (dots) and calculated (solid lines) resonance fields of the FMR and SWR modes for the different NC diameters. The black solid line is a fit to an average of the FMR mode for all three devices. Inset: A plot of the fitted NC diameter (D') vs. the nominal diameter (D), together with a line indicating $D' = D$.

3.1.4 Fit frequency-field dependency of satellite peak with dispersion relation

The frequency versus field dependence of the measured FMR and SWR modes is summarized in Figure 3.4. The black solid line shows the average behavior of the FMR mode for all three NC diameters, essentially reproducing Figure 3.1. For a fixed frequency, we find that the SWR mode shifts to lower fields as the NC diameter decreases. Assuming that the origin of the SWR mode lies in the exchange interaction, the diameter of the NC, D', can be estimated using the dispersion relation, Equation (1.12). The room temperature value of the exchange stiffness is set to $A = 11$ pJ/m [86]. The estimated sizes of the NCs are in reasonable agreement with the corresponding nominal values, as shown in the inset to Figure 3.4.

3.1.5 Micromagnetic simulations

Micromagnetic simulations were performed using the mumax3 solver [87]. Since the actual spin-valve mesa is too large to be simulated in its entirety in a reasonable time frame, calculations are limited to a 5.120 μm $\times$ 2.560 μm $\times$ 4 nm volume with periodic boundary conditions tailored to mimic the lateral aspect ratio of the experimental spin-valve mesa.

To break the symmetry of the system, which might otherwise entirely prevent any STT-related effects and nonconservative SW scattering, the applied field is assumed to point 5° out of plane, comparable to the possible error in the experimental field alignment. As a first step, the evolution of the ground state of the entire Co/Cu/NiFe stack is calculated, confirming that (i) the Co and NiFe layers remain virtually collinear in the given range of the applied magnetic fields, and (ii) there are no mutual stray fields produced between the layers in the vicinity of the NC. Since there is a significant spin wave-dispersion mismatch between Co and NiFe, any resonant dynamic magnetic coupling between the layers is not expected. Under these three considerations, the dynamics of the NiFe free layer is simulated alone.

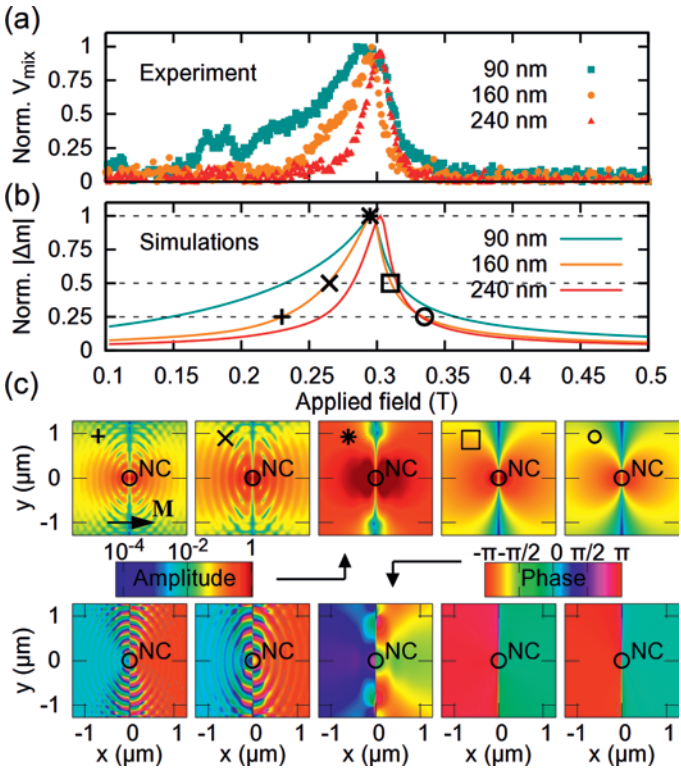

Figure 3.5: (a) Normalized measured mixing voltage (V_{mix}) and (b) normalized simulated magnetization precession amplitude for the three NC diameters as a function of the applied in-plane magnetic field. (c) Spatial maps of magnetization precession amplitude (top row) and phase (bottom row) simulated for a $D = 160$ nm NC diameter taken at the fields corresponding to the main peak and its 12 and 14 heights (as shown by the corresponding black symbols in (b)). Propagating spin waves are clearly seen for the two lowest fields.

In the simulations, the experimental data acquisition routine is replicated by performing the field sweeps with a harmonic excitation of $f = 18$ GHz. The infinite wire approximation was used to calculate the Oersted field produced by the NC [88, 19]. For every value of the applied field, the system is allowed to reach the steady state, before sampling the spatial map of the magnetization for the following 5 ns at 3.5 ps time intervals with a subsequent pointwise FFT applied and the amplitude and phase of the magnetization precession extracted at the excitation frequency. Where applicable, the direction of the spin-current polarization was assumed to be collinear with the magnetization in the nominally fixed Co layer. The set saturation magnetization, gyromagnetic ratio, and damping constant were estimated by fitting a Kittel equation to the experimental data. The room temperature value of the exchange stiffness was set to $A = 11$ pJ/m [86].

3.1.6 Anisotropic nature of spin waves propagation

The simulated magnetic response shown in Figure 3.5(b) agrees well with the experimentally measured data shown in Figure 3.5(a). To identify the origin of the observed peak asymmetry, the spatial profiles of the magnetization precession amplitude in the vicinity of the resonance is investigated(see Figure 3.5(c)). The snapshots clearly show that SWs propagate on the low-field side of the main peak, while no SWs are resolved on the high-field side. Looking closer at the phase profiles of the corresponding modes, which essentially depict the wavelength of the excited magnons, the following conclusions can be made: (a) the propagation of SWs perpendicular to the saturation direction is suppressed and (b) the lowest excited mode is not uniform, but rather antisymmetric with respect to the NC center.

3.1.7 Dependence of coexistence band of magnetostatic and exchange-dominated SWs on the thickness of FM layer

If the free layer is magnetized in-plane, then both backward volume magnetostatic SWs (BVMSSW) and surface magnetostatic-exchange SWs (SMSSW) can be excited: see Equations (1.9) and (1.10), which are calculated for propagation along and perpendicular to the saturation direction, respectively. The exchange contribution is included by substituting $B \to B + \mu_0 M_s \left(\lambda_{ex} k\right)^2$.

The corresponding dispersion relations are shown in Figure 3.6 for a Py thicknesses, d, of 100 nm (green lines) and 4.5 nm (red lines). There is always a region of resonance fields where magnetostatic and exchange-dominated SWs coexist, as highlighted by the shaded area in Figure 3.6 for the Py thickness of 100 nm. Although the band is broad for relatively thick layers, it only amounts to 1.16 mT for the 4.5 nm Py—i.e., an order of magnitude smaller than the intrinsic broadening of the FMR peak. We therefore conclude that the SWs contributing to the low-field tail of the FMR peak are exchange-dominated. Note that the calculated dispersion relations differ from what is found using Equation (1.12) (the thick solid line in Figure 3.6). This difference arises as the dispersion relations also

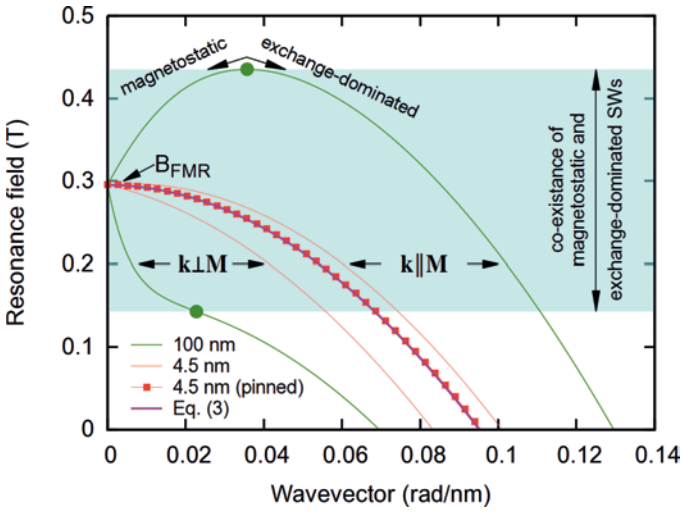

Figure 3.6: Dispersion relations for SWs propagating parallel and perpendicular to the saturation direction for the different thicknesses of the NiFe layer. The points correspond to the minimum of the SW group velocity.

strongly depend on the exact boundary conditions at the free layer surfaces. For instance, if the NiFe film is pinned on both surfaces—that is, if it is placed between sufficiently thick metallic layers—the dispersion of the exchange-dominated backward volume SWs is given by the following equation (shown by the dotted line in Figure 3.6) [89]:

$$f_{\text{BVMSSW-pinned}} = \left[\left(f_B + f_M \left(\lambda_{ex} k \right)^2 \right) \times \left(f_B + f_M \left(\lambda_{ex} k \right)^2 + \frac{f_M}{1 + (kd/\pi)^2} \right) \right]^{1/2} \tag{3.1}$$

Note that, in this case, the spectrum of the exchange-dominated surface SWs will be dispersionless and experimentally inaccessible.

Since Equation (1.12) fits the NC diameter reasonably well, we conclude that (a) the detected mixing voltage is generated by the exchange-dominated backward volume SWs and (b) there is undoubtedly some surface pinning of the NiFe layer. Determining the exact origin of the pinning and its strength are beyond the scope of the present study.

3.1.8 Oersted field: the main origin of magnetodynamics

Due to the collinear free and fixed layers, we do not expect any significant contribution from the ST to the observed magnetization dynamics; this is confirmed by comparing micromagnetic simulations including and excluding ST. Correspondingly, for the in-plane applied magnetic fields in the NC geometry with no *dc* bias currents applied, the rf Oersted field is the primary excitation mechanism responsible for the observed dynamics.

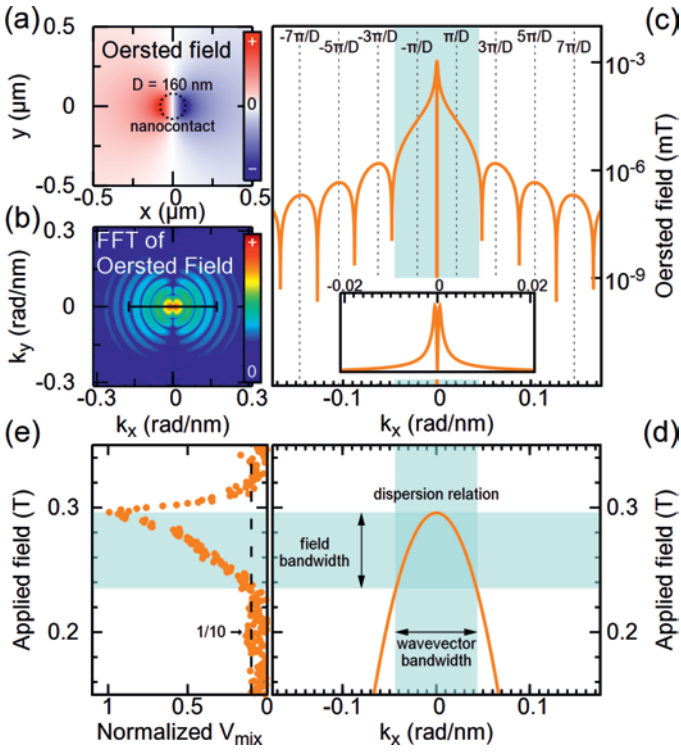

Figure 3.7: (a) The spatial distribution and (b) the corresponding 2D FFT of the out-of-plane component of the Oersted field by the $D = 160$ nm diameter NC. (c) The Oersted field as a function of the wavevector component along the saturation direction is shown for the $D = 160$ nm diameter NC. The inset shows a zoom-in of the small wavevector part of the spectrum. (d) Dispersion relation of the exchange-dominated SWs. (e) Experimentally acquired magnetization dynamics spectrum using a nanocontact of $D = 160$ nm diameter.

In a linear approximation, the response of the system is essentially determined by the spectrum of the excitation, which in our case is provided by the rf Oersted field. If the excitation has a finite amplitude at some point of the reciprocal space (i.e., at the given frequency and wavevector) then the corresponding magnon will be excited, if allowed. The spatial profile of the Oersted field and its spectrum for the $D = 160$ nm NC are shown in Figure 3.7(a) and (b), respectively. We can identify both local and global antisymmetries with respect to the NC center with corresponding periods determined by twice the NC diameter and mesa width, L, respectively. Since both spatial components are naturally confined to their unit periods, the linewidth of the corresponding excitation peak is finite. The Oersted field thus couples most efficiently to the SW bands with widths of $2\pi/L$ and

π/D corresponding to the wavevectors of $2\pi/L$ and $n\pi/D$, respectively, where $n = 1, 3, ...$ (see Figure 3.7(c) and its inset). As the NC diameter decreases, the position and width of the former band stay constant, while the latter band shifts towards lower resonance fields and increases its width, leading to the observed extension of the tail in the excitation spectrum.

It is important to mention that the circular NC cannot effectively couple to the uniform FMR. Instead, the main peak observed in the experiments and simulations corresponds to the antisymmetric mode with $k = 2\pi/L$. However, due to the vanishing magnetostatic dispersion, its resonant field is virtually indistinguishable from the uniform $k = 0$ FMR mode.

3.1.9 The place of cut-off wave vector in SW bands

Considering a typical FMR experiment where the excitation frequency is fixed, according to Equation 1.12, the wave vector of the generated propagating SW is ultimately determined by the value of the applied magnetic field. As the field is swept towards zero, past the dominant FMR resonance, the NC continuously excites propagating SWs of increasing wave vectors. Since the excitation amplitude drops rapidly for low values of the applied field (i.e., for short wavelength SWs), the detected magnetic signal vanishes accordingly, leading to the appearance of the low-field tail (Figure 3.7(c) and (e)).

By estimating that the extent of the tail is at one-tenth of its peak amplitude, we can project the corresponding experimentally observed applied magnetic field to the cut-off wavevector of the excitation spectrum, as schematically demonstrated by the shaded rectangles in Figure 3.7(c), (d), and (e). This gives us the cut-off wavevectors (in units of π/D') of 1.93, 1.95, and 2.34 for the NCs of 90, 160, and 240 nm nominal diameters, respectively. Since these values fall roughly inside the first two fundamental SW bands attributed to $k = 2\pi/L$ and $k = \pi/D$, the two-peak scheme used to fit the experimental data is fully justified.

3.1.10 NC diameter dependence of the FMR and SWR inhomogeneous broadenings

Finally, the NC size dependence of the FMR and SWR inhomogeneous broadenings shown in Figure 3.3 can be well understood by assuming that they are inherited from the linewidth of the corresponding excitation peaks. For the SWR mode, the expected extrinsic contribution to the magnonic linewidth is 96 mT, 43 mT, and 15 mT, respectively, for NC diameters of 82 nm, 122 nm, and 205 nm; this is in excellent agreement with the fitted values. In contrast, for the FMR, the contribution is vanishing and should be virtually independent of the NC size. However, if the NC had shape imperfections, the corresponding irregularities in the Oersted field profile should broaden the excitation peaks and, eventually, the FMR and SWR. As we typically observe a less perfect NC for smaller diameters, the inhomogeneous broadening of FMR should increase accordingly, consistent with the experimental data.

3.1.11 Conclusions

In conclusion, using ST-FMR techniques, an in-depth study of the magnetodynamics is provided in a quasiconfined system—namely, an NC patterned on an extended pseudo-spin-valve film stack. The observed spectra are highly asymmetric and cannot be explained by a single resonance mode, as has been done in the past [78, 75]. Instead, each spectrum is fit by a combination of two Lorentzians, from which the FMR mode resonance field and linewidth can be extracted. The secondary mode corresponds to the generation of exchange-dominated spin waves with a wavevector inversely proportional to the NC diameter. The results are reproduced by micromagnetic simulations that show that the rf Oersted field generated by the injected rf current is the dominant excitation mechanism of the observed magnetization dynamics. In this way, we experimentally demonstrate a highly tunable point source of the propagating SW with the wavevectors limited only by the resolution of the fabrication process used. This is of paramount importance for the applications of sub-THz and THz magnonics and spintronics.

3.2 Tuning exchange-dominated spin-waves using lateral current spread in NC-STO

3.2.1 Another method for changing the distribution of Oersted field

In previous work, the Applied Spintronics group investigated how the current distribution depends on the copper thickness of the bottom electrode (t_{Cu}) in NC-STNOs based on Co/Cu/NiFe stacks [90]. It is found that increasing t_{Cu} from 10 to 70 nm results in a 40% reduction in the threshold current, an order of magnitude higher microwave output power, and close to two orders of magnitude better power conversion efficiency.

In this study, we apply the theory from the previous section in order to tune the spin-wave resonance mode by changing the current distribution and, as a result, the distribution of Oersted field (H_{Oe}). We do this by varying the thickness of the bottom electrode. We use the same multilayer stack configuration as before, except that we change the thickness of the bottom Cu layer. We measure the rectified spectra in an in-plane magnetic field and compare the results with simulations.

3.2.2 Study of spin wave spectra of Py with different thicknesses of bottom electrode

The structure of pSV is the same as previously, except for the thickness of bottom electrode: substrate / Pd (8 nm) / Cu (t_{Cu}) / Co (8 nm) / Cu (8 nm) / $Ni_{80}Fe_{20}$ (4.5 nm) / Cu (3 nm) / Pd (3 nm) with t_{Cu} = 10, 30, and 70 nm. The nanocontact size is chosen D =250 nm. The ST-FMR measurement configuration is the same as before; the rf power was maintained at a constant low value of −10dBm to ensure that the excited magnetodynamics was in the linear regime. The measurements were performed at a fixed excitation frequency, f = 18 GHz, while the in-plane applied field was swept from 0 to 0.5 T. Five nominally similar devices were measured and the spectra presented in Figure 3.8 is the normalized mean value of those five spectra per sample.

3.2.3 Experimental results

Figure 3.8 shows the normalized mean value of ST-FMR spectra measured at a fixed frequency of 18 GHz for five devices on each of three samples with t_{Cu} = 10, 30, and 70 nm. The solid lines are fits of two symmetric Lorentzian to the NiFe peak (peak at higher fields). Based on the previous section, the effective diameter (D') can be estimated using the dispersion relation, Equation (1.12).

Focusing on the free layer (NiFe) mode, the extracted effective diameter from the fit is presented in Figure 3.9. It can be seen that, by increasing t_{Cu}, the mean effective diameter decreases monotonically and is inversely proportional to the mean linewidth,

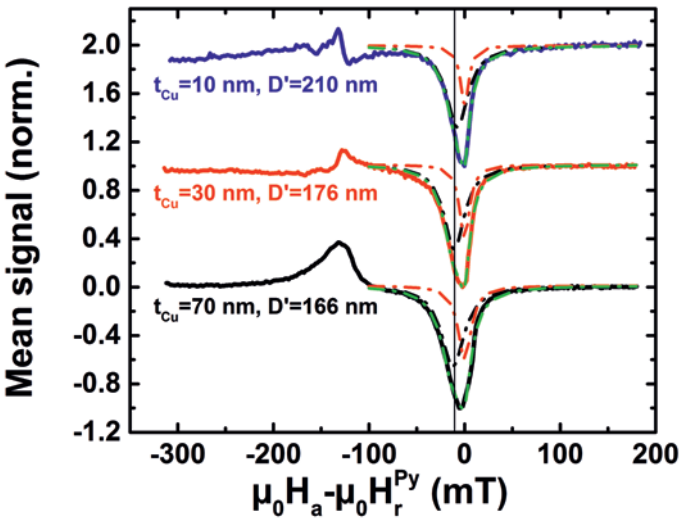

Figure 3.8: (a) Normalized mean ST-FMR spectrum of the $D = 250$ nm device taken at $f = 18$ GHz and $P = -10$ dBm for three different thicknesses of Cu bottom layer, together with a fit (black line line) based on two Lorentzians, as described in Ref.

(inset to Figure 3.9). In the previous section [91], we showed that the bandwidth of the SW package is proportional to the effective diameter.

3.2.4 COMSOL simulation

The theory extracted in the previous section predicts that the effective diameter is defined by the Oersted field. To test this hypothesis, we investigated how the current redistributes and induces H_{Oe}. To calculate the current flow and H_{Oe} in each layer of the device, COMSOL Multiphysics simulation software is used with a detailed three-dimensional finite-element model of the NC-STNOs. The input values of the nanocontact size and Cu thickness were $D = 250$ nm and $t_{\mathrm{Cu}} = 10$, 30, and 70 nm, respectively.

[90] show that the current from the top contact first crowds along the perimeter of the NC, and then spreads out laterally; by increasing t_{Cu}, the lateral current spread can be strongly reduced. Figure 3.10 (a) and (b) show that the Oersted field increases for thicker t_{Cu}—i.e., when the current spread is reduced. In Figure 3.10(c), this amplification is highlighted in the ferromagnetic layers by plotting the average strength of H_{Oe} in the middle of the NiFe ($H_{\mathrm{Oe}}^{\mathrm{NiFe}}$) and Co ($H_{\mathrm{Oe}}^{\mathrm{Co}}$) layers under the NC, normalized by $H_{Oe,(t_{\mathrm{Cu}}=70\ \mathrm{nm})}^{\mathrm{NiFe}}$.

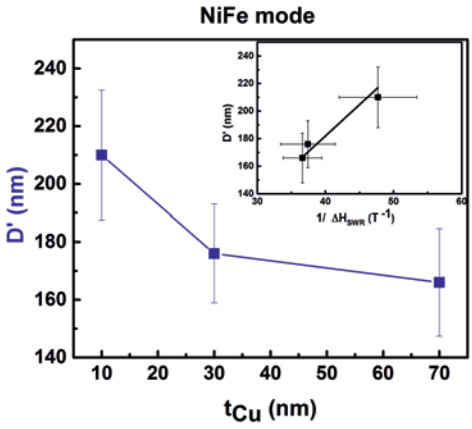

Figure 3.9: Mean value of effective diameter (D') vs. thickness of Cu bottom layer. Inset: Plot of mean values of effective diameter (D') vs. mean linewidth of SWR mode extracted from measurement of five devices.

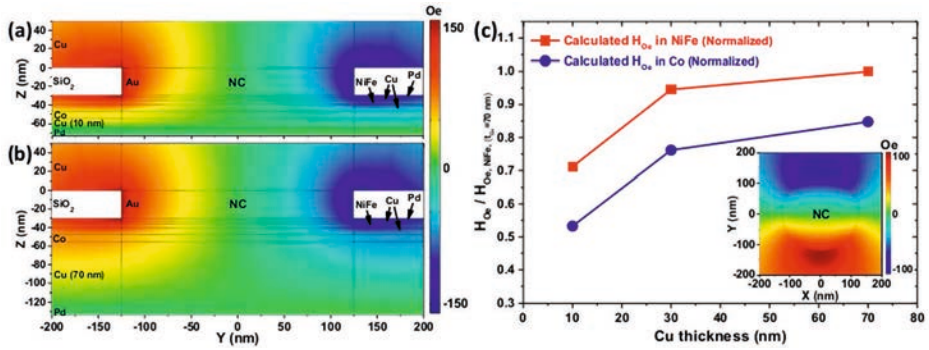

Figure 3.10: (a) Detailed x component of H_{Oe} induced by perpendicular current in all layers for $t_{\mathrm{Cu}} = 10$ nm. (b) The same for $t_{\mathrm{Cu}} = 70$ nm. (c) Calculated average strength of H_{Oe} induced by perpendicular current under the NC in the middle of NiFe and Co layers, normalized by $H^{\mathrm{NiFe}}_{Oe,(t_{\mathrm{Cu}}=70\ nm)}$. Inset shows the top view of the middle of the NiFe layer, of which the colored map indicates the x component of H_{Oe} for $t_{\mathrm{Cu}} = 70$ nm. All results are for $D = 250$ nm.

The results show that by increasing t_{Cu} from 10 to 70 nm, the strength of the $H^{\mathrm{NiFe}}_{\mathrm{Oe}}$ and $H^{\mathrm{Co}}_{\mathrm{Oe}}$ undergo remarkable increases of ∼30% and ∼60%, respectively, under the NC geometry. This large increase is caused by the more uniform distribution of the Oersted field in the devices with thicker t_{Cu}. The Oersted field plays a key role in exciting the

dynamics, and the decrease in the effective diameter with increasing Cu thickness (Fig. 3.10(b) must accordingly be a result of a more uniform Oersted field distribution. We can therefore conclude that it is possible to tune the SWR by tailoring the lateral current.

3.2.5 Conclusions

In conclusion, I have studied the tuning of spin-wave resonance excitation in nanocontact spin-torque oscillators. Our findings show that by changing the spread of the lateral current, the spatial characteristics of the resulting spin-wave beams can be controllably tuned. The effective diameter (which is inversely proportional to the mean of the wavevector) decreases with increasing Cu bottom layer thickness. It can be concluded that the spread of current must be greater for the lower thickness of the Cu underlayer at the NiFe site, which our simulation results also confirm. The spin-wave resonance linewidth increases with the increasing thickness of Cu bottom layer. This is connected to the first conclusion and confirms the theory presented in Section 3.1.

Chapter 4

Exchange coupling between two FM layers

The systematic variation of the strength and oscillation period of indirect magnetic exchange coupling (IEC) between adjacent ferromagnetic layers in a multilayer structure has been studied for a decade [92, 23, 93, 28, 94, 32], due to its potential application in giant magnetoresistance (GMR) based read heads and magnetic random access memory (MRAM). In FM/NM/FM trilayer structures, the material and thickness of the interlayer play the key role in the type of interlayer coupling, which may be either ferromagnetic (FM) or antiferromagnetic (AFM).

In exchange-coupled samples, the optical mode is normally only observable when the coupled layers have different resonance frequencies (f_{FMR})—e.g., as a result of having different saturation magnetizations or anisotropies—although it is also possible to detect this mode for identical layers using so-called longitudinal FMR[94].

Spin pumping in coupled layers has been extensively studied [95, 96, 97, 98], but the majority of those investigation have focused on the regime where the static coupling between the layers is very weak or on one or a limited number of frequencies.

In this chapter, based on Co/Cu(t)/Py trilayers with t_{Cu} in the range from 0 to 40 Åand with help of broadband conventional FMR measurement, I first study the interplay between the static and dynamic interlayer exchange within the in-plane applied field. In this case, field–frequency dependency of the modes do not coincide with each other, except at zero field-frequency. I focus on the variation of spin pumping and IEC with the thickness of interlayer and also with the range of applied field. Based on exchange coupling values extracted from the analysis, samples are categorized into four regimes: strong, intermediate, weak, and zero coupling.

Second, based on the same set of samples and with the help of broadband conventional FMR measurement, I am focused on the collective dynamics of the trilayer when the FMR frequencies of the separate layers form a cross-point (CP) at a particular value and angle of the applied magnetic field, while being substantially different otherwise. To achieve this goal, the field is applied with the angle $\theta = 82^{\circ}$, where CP takes place at $\mu_0 H = 1.15T$, $f = 13GHz$.

Finally, in last section, I study the magnetodynamics in a nanocontact (NC) on Co/Cu(t)/Py pSV for t_{Cu}= 20 Åby taking t_{Cu}= 80 Åas a reference sample in the same configuration of applied field in second section—i.e. with $\theta = 82°$. I excite the Co/Cu/Py NC-STO system with rf current using the ST-FMR measurement technique and characterize the observed features.

4.1 Tunable spin pumping in exchange-coupled magnetic trilayers

4.1.1 Fit of individual layers with Kittel equation

The FMR measurements were performed by sweeping the external in-plane field at fixed frequencies, varied step-wise from 3 to 37 GHz. A fit of the derivative of an asymmetric Lorentzian, Equation (2.6), to the signal provides the resonance field ($\mu_0 H_r$), the full-width half-maximum (ΔH), and the amplitude (A) of the absorption peak. The Kittel equation [99], Equation (2.3), was subsequently fit to the resonance frequencies of the single layer samples:

The results of the fits gave the following magnetic properties of Py: $\gamma/2\pi$=29.0 GHz/T and $\mu_0 M_{\text{eff}}$=0.89 T and of Co: $\gamma/2\pi$=30.8 GHz/T and $\mu_0 M_{\text{eff}}$=1.56 T. The additional fields are on the order of 2 mT for both samples.

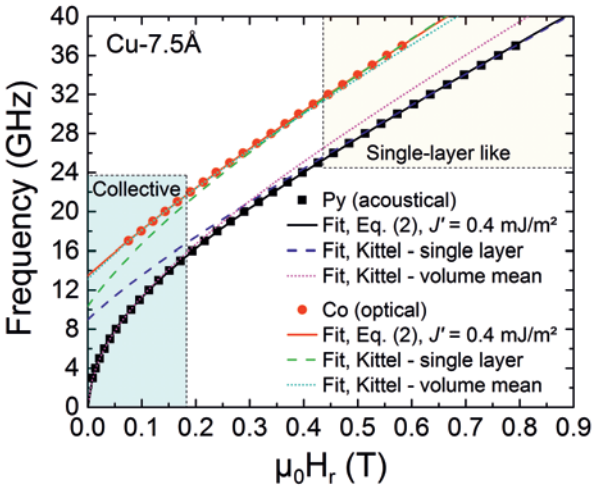

Figure 4.1: FMR frequency as a function of field for the Cu-7.5 Åsample. The data (filled symbols) is compared to three different models. The behavior at all field values is well described by a fit of Eq. 1.18 to the data, using $J' = 0.4$ mJ/m^2. The transition from collective to single-layer-like precession is illustrated by two fits using the Kittel equation, where the magnetization and gyromagnetic ratio are fixed either to the values of single Py and Co, or to the volume mean of these layers. The effective field was used as a free parameter.

4.1.2 Fit of multilayers with free energy numerical model

For multilayers, we used a numerical model (1.18) to fit the data. We have followed the equations presented in Ref. [30] and [31], and the results show a clear correspondence

with the data (see Fig. 4.1). Nevertheless, the Kittel equation still sheds some light on the nature of the oscillations. At high fields, the frequency follows the predictions using the magnetization and gyromagnetic ratio of the single films, while the trend of the low f_r matches the behavior of an effective medium with an M_{eff} and γ given by the volume average of the two materials. This implies a transition from a region (low f_r) governed by collective motion to one where the inherent properties of each layer dominates.

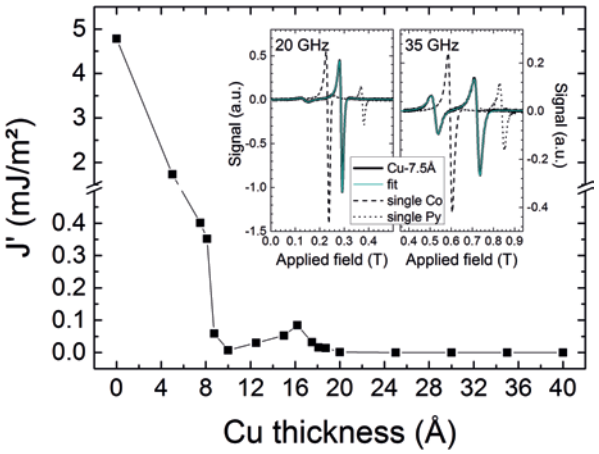

Figure 4.2: The interlayer exchange coupling (J') as a function of spacer layer thickness. J' was determined by fits of Eq. 1.18 to the field dependence of the FMR frequency. Inset: FMR spectra of Cu-7.5 Å(thick black lines) together with fits of two asymmetric Lorentzians (cyan lines), and the spectra of the single layer Co (dashed lines) and Py (dotted lines). The left and right plots show the absorption at 20 and 35 GHz, respectively.

4.1.3 The positive oscillatory behaviour of interlayer coupling

The derived values of the interlayer coupling are presented in Figure 4.2. The layer thicknesses and magnetizations were fixed during the fits to Eq. 1.18, while we let J', γ^{Py}, and γ^{Co} vary. The resulting values of the IEC were essentially unchanged if the gyromagnetic ratios were treated as constants, but the goodness-of-fit was worse. The coupling is ferromagnetic for all t_{Cu}, in contrast to the familiar behavior where J' is expected to oscillate between positive and negative values. We can therefore conclude that the interactions between the layers are not only given by RKKY interactions, but also include Néel (orange peel) coupling [100]. This interpretation is strengthened by the fact that we observe a minimum at the thickness (1 nm) where a negative maximum would otherwise be expected [101, 102].

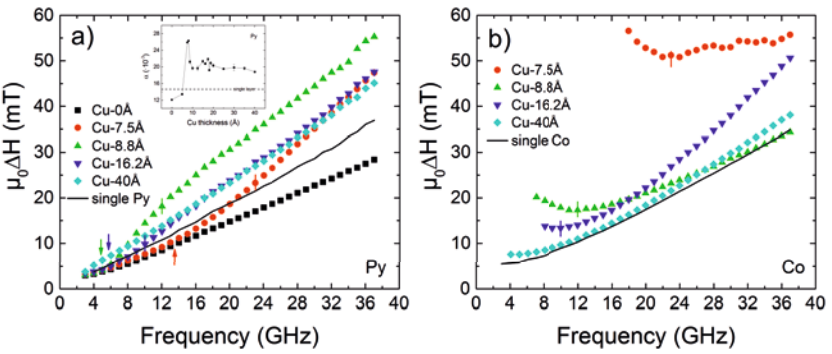

Figure 4.3: Linewidth vs FMR frequency for the a) Py and b) Co resonances. The vertical lines in both a) and b) mark the inflection point of the Co linewidth, which is a measure of the transition from collective to single-layer-like behavior. The arrows show the Co-frequency at zero applied field. Below this frequency, there is only one resonance in the system.

4.1.4 The effect of IEC on linewidth of low frequency resonance modes

The linewidth of the Py and Co resonances are shown in Figure 4.3a and b, respectively. For samples in the intermediate or weak coupling regime, both datasets have a distinct concave shape, which is more pronounced for Co. The linewidth of Co not only flattens out, but also increases at low frequencies. The optical mode is expected to have a much larger linewidth than the acoustical mode, due to spin pumping [103]. However, the linewidth of the single layer Co is not Gilbert-like, but rather saturates at a constant value. This behavior is inherited in the bilayer samples. The damping of the Co mode also fluctuates significantly with Cu thickness, probably due to strain-induced effects beyond our control. We have consequently chosen not to dwell on the behavior of the linewidth associated with this material, but we do note that the increase in ΔH is consistent with an optical character of the mode.

If we follow ΔH^{Py} ($J' > 0$) from high to low frequencies, we see that the initial constant slope is reduced at a certain frequency marked by a vertical line in the figure. It is noteworthy that this frequency (f_{infl}) also corresponds to the inflection point of the Co linewidth (Fig. 4.3b). The relative resonance intensities (see Fig. 4.4) also change drastically around f_{infl}. Both these effects are clear signs of a transition from a high-frequency region where the acoustic and optical modes are mostly associated with the Py and Co layers, respectively, to a low-frequency region where the precession is truly collective. The linewidth of the acoustic mode decreases, since it represents in-phase oscillations and the spin currents cancel, while they add up in the optical out-of-phase mode. The Co linewidth increases accordingly. When the Co (optical) mode disappears, marked by arrows in the figure, the slope again become constant and follows the single film behavior. The absence

of nonlocal damping implies that both layers precess in phase and that the sum of the spin currents is virtually zero [26].

The Cu-40 Årepresents the samples without interlayer coupling; in such systems, the linewidth is linear in f, as expected for a pure spin-pumping effect. The inset in Figure 4.3a shows the damping parameter of Py extracted from the linear region at high frequencies. The damping shows a weak dependence on J' above the spin relaxation coherence length (≈ 1 nm). Nonetheless, since α is constant for samples with no coupling, it is obvious that the main source of the increased damping is spin pumping.

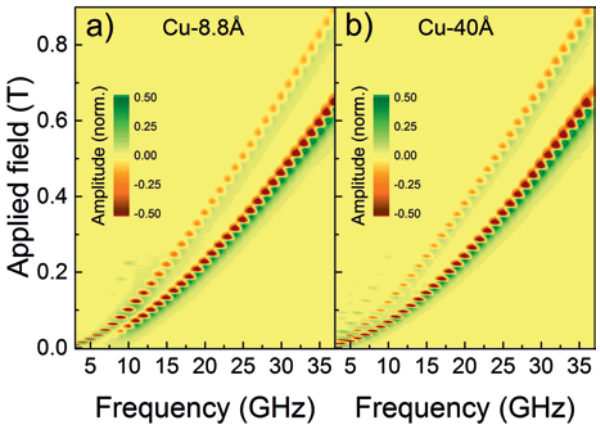

Figure 4.4: Color map of the FMR for a) a sample with weak and b) zero interlayer coupling. The Py amplitude is lower than that of Co for all frequencies when the layers are decoupled (b). However, in the presence of IEC, the relative intensities change below 15 GHz (a). The modification of the intensities mirrors the transition from single-layer-like behavior at high frequencies/fields, to a region where the precession is truly collective with acoustic (high amplitude) and optical (low amplitude) modes.

4.1.5 Study amplitude of the modes - transition to collective regime

The measured spectra (3–37GHz) of the Cu-8.8 Åand Cu-40 Åsamples are presented in Figure 4.4a and 4.4b, respectively. The intensity of the signal is dependent on both the probed magnetic moment and the frequency. We have therefore normalized the amplitude at each frequency. The Co mode of the Cu-40 Åsample is stronger than the Py mode at all frequencies, as expected considering the smaller magnetization and thickness of the Py layer. The presence of interlayer coupling gives a different picture. For Cu-8.8 Å, the amplitude of the Co mode quickly decreases below ≈ 15 GHz. This reveals the transition to a region where the Py and Co show distinct acoustic and optical mode characteristics, in accordance with the interpretation of the frequency dependence of the damping.

4.1.6 Conclusion

In this study, I investigated the interplay between IEC and spin pumping, using Co/Cu/Py pseudospin values. I showed that the hybridization between the layers, leading to acoustical and optical modes, is not only dependent on the IEC, but also on the field and frequency. The collective nature of the precessions is clear at low fields, as reflected by the relative amplitudes and the field dependence of the resonance frequencies. At higher applied fields, the layers behave as single films subject to an effective field proportional to the interlayer coupling. This transition, from collective to single layer precession, is accompanied by changes in the slope of ΔH vs. f, (i.e., the damping), and I attribute those changes to the spin pumping between the layers. The results demonstrate that it is possible to engineer a *cut-off frequency*, below which the spin pumping is effectively turned off.

4.2 From individual to collective behavior in multilayered magnetic structures in the vicinity of the resonance coincidence point

This section is organized as follows: First, I describe our experiment and model details, then I show the colormap plot of the field-frequency dependency of three samples (each representative of one regime), and finally I study the linewidth and amplitude behavior of the modes in each regime in comparison with individual layers and fit with the Franco model (see Section 1.2.4).

4.2.1 Experiment and numerical model of Kittel equation for fit in an oblique field

The FMR measurements were carried out in the range of f = 2–20 GHz. I fixed the nominal angle between the field and the sample plane to 82°. This angle was chosen to obtain a coincidence point of the Co and NiFe resonances in a frequency and field range well within the limits of the setup. The sample structure and measurement configuration is illustrated in Figure 4.5.

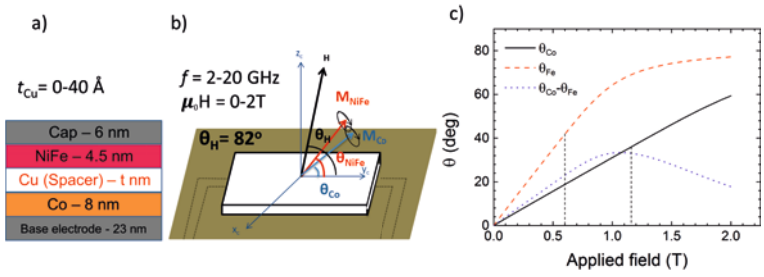

Figure 4.5: a) Schematics of the sample structure and b) the FMR setup configuration. c) Calculated angles of the magnetization in single Co (red solid line) and NiFe (black dashed line) layers using Eq. 2.4. The blue dotted line shows the difference between the two angles; the vertical dashed lines marks the field of the linewidth maxima.

The FMR signal was fit using equation (2.6). The FMR frequency of a thin magnetic film can be described by equations (2.4) and (2.5). The result of fit to the single layers are: $\mu_0 M_{\mathrm{Co}} = 1.68$ T, $\gamma_{\mathrm{Co}}/2\pi = 29.2$ GHz, and $\mu_0 M_{\mathrm{NiFe}} = 0.81$ T, $\gamma_{\mathrm{NiFe}}/2\pi = 28.3$ GHz. The actual field angle was treated as a free parameter and the best fits were obtained for $\theta_{\mathrm{H}} = 83.5°$—i.e., very close to the nominal value (Fig. 4.5(c)). The anisotropy was assumed to be zero. The extracted parameters were subsequently used to calculate the internal tilting angles of the magnetizations in uncoupled layers (Fig. 4.5). The maximum relative

angle $\theta_{\mathrm{NiFe}} - \theta_{\mathrm{Co}} = 33°$ occurs at a field ($\mu_0 H_{\mathrm{ext}} = 1.05$ T), close to the experimentally determined CP at $\mu_0 H_{\mathrm{CP}} = 1.15$ T.

4.2.2 Numerical model for exchange coupled multilayers

The strength of the IEC is determined in the present samples in Section 4.1 using in-plane measurements; the samples were divided into four groups of different coupling strength: strong, intermediate, weak, and zero coupling. Although the strong and intermediate regimes display very similar behavior in this study, I have chosen to keep the same notation for consistency, the only exception being that I call the last category "very weak" to highlight that the samples may have a tiny residual coupling. The model employed to fit the value of J' in this study is one recently developed by Franco and Landeros [32], but the results are similar to those from the previous section. The parameters extracted from the fits of the Kittel equation (2.4) to the data of the single layers were used as fixed input parameters and J' is the only free variable in the subsequent fits utilizing the model in Ref. [32].

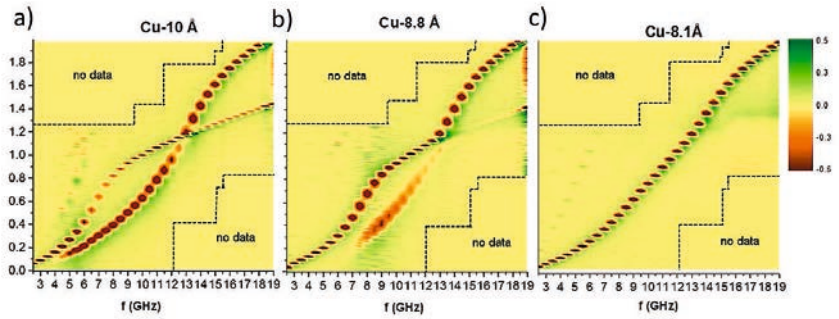

Figure 4.6: Color maps of the FMR spectra of samples with spacer layer thickness (a) $t_{\mathrm{Cu}} = 10$ Å, (b) $t_{\mathrm{Cu}} = 8.8$ Å, (c) $t_{\mathrm{Cu}} = 8.1$ Å. Signal strength is normalized to -1 at each frequency to highlight the relative intensity of the modes. Note: the weak feature in Cu-8.1 Å, which appears above 13 GHz, is not the optical mode, but an unidentified mode.

4.2.3 Three distinctly different regimes

The raw FMR data of selected samples, representing three regimes of coupling strength, is presented as colormaps in Figure 4.6. The different sample categories demonstrate distinctly different behaviors: the Cu-10 Åsample has two modes, which keep their respective character after the CP; the acoustical and optical nature of the modes in the Cu-8.8 Åsample is indisputable; the Cu-8.1 Åsample has only one mode in the measured

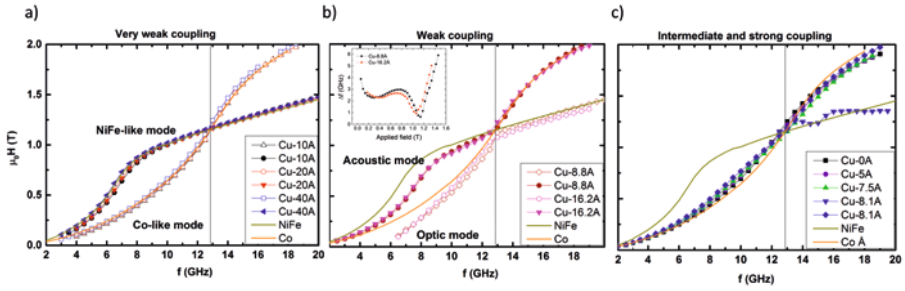

Figure 4.7: Resonance field ($\mu_0 H_r$) as a function of frequency (f). The open symbols denote Co/optical modes, while the closed symbols show the NiFe/acoustical modes. The inset in (b) shows $\Delta f = f_{op} - f_{ac}$ versus field. The Cu-8.1 Åmode indicated by the blue triangles is neither an acoustical nor an optical mode, but an unidentified mode.

field and frequency range. This sample also displays a weak feature above the CP. We have not been able to identify this mode, but include it in the following figures for completeness.

4.2.4 Field-frequency dependency characteristics of each regime

The different behavior in the three regimes is further emphasized in Figure 4.7, where the resonance fields are presented. It is indeed possible to roughly estimate the strength of the IEC merely by inspecting the data. The stronger the coupling, the larger the shifts to lower resonance fields compared to the single layers. It is, however, not easy to distinguish which of the two samples in the weak coupling regime has the highest IEC. The acoustical modes follow each other closely, while the shift in the optical mode is higher for Cu-8.8 Åbefore the CP and smaller above. Trilayers with a notable IEC exhibit a frequency gap, which increases with increasing J'. The inset in Figure 4.7(b) shows the frequency difference between the optical and acoustical modes ($\Delta f = f_{op} - f_{ac}$) as a function of applied field (i.e., the resonance field). The larger frequency gap of Cu-16.2 Åshows that the IEC is stronger in this sample than in Cu-8.8 Å.

The observed frequency shift of both modes is always higher before the CP than after. We calculated the frequency shift to elucidate this point. The results are found in Figure 4.8 and show that the optic mode continuously shifts to higher frequencies as J' increases. The acoustic mode, on the other hand, is limited by a maximum frequency before the coincidence point and only exhibits tiny shifts after the CP. The calculations do not explain the inconsistent shifts mentioned in the paragraph above, and this might imply that the Co layers in the two samples are not completely identical.

The IEC strength of the samples was determined by fits using the model presented in Ref. [32] (see Fig. 4.9). The model captures the experimental results well when J' is small, but deviates more as the coupling increases. Nonetheless, the estimated values allow us to

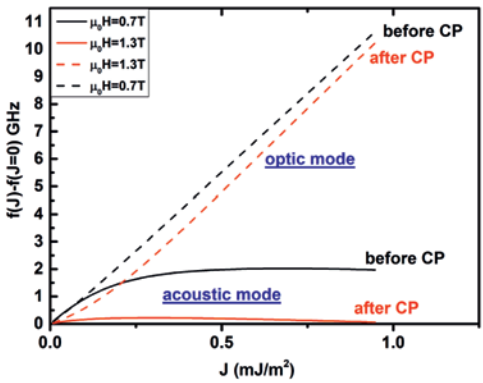

Figure 4.8: Calculated frequency shift due to interlayer exchange coupling (J') for the acoustical (solid lines) and optical (dashed lines) modes. Two different fields are compared, $\mu_0 H = 0.7$ T (black lines) and $\mu_0 H = 1.3$ T (red lines), representing resonances that occur before and after the coincidence point (CP).

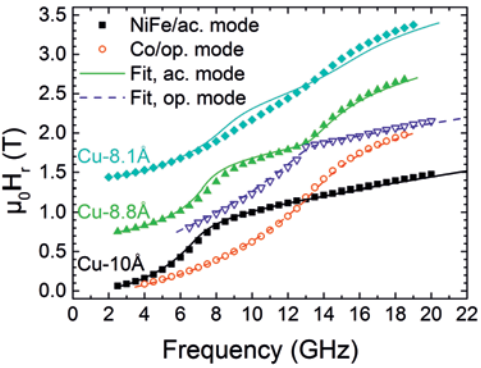

Figure 4.9: Fits of the model given in Ref. Franco2016 (lines) to the data (symbols). The NiFe/acoustical resonance fields are presented by solid symbols, while the Co/optical modes are denoted by open symbols. The data for Cu-8.8 Åand Cu-8.1 Åare offset by 0.7 and 1.4 T, respectively. The fitted values of J' are 0.016, 0.07, and 0.87 mJ/m^2 for the Cu-10Å, Cu-8.8Å, and Cu-8.1 Åsamples, respectively.

quantify the coupling strength in the different regimes: crossing of the modes occurs for $J' < 0.02$ mJ/m^2 (very weak IEC), clean optical modes are observed when $J' \approx 0.1$ mJ/m^2 (weak IEC), and they are pushed far away from the Co resonance for coupling strengths higher than $J' \approx 0.8$ mJ/m^2.

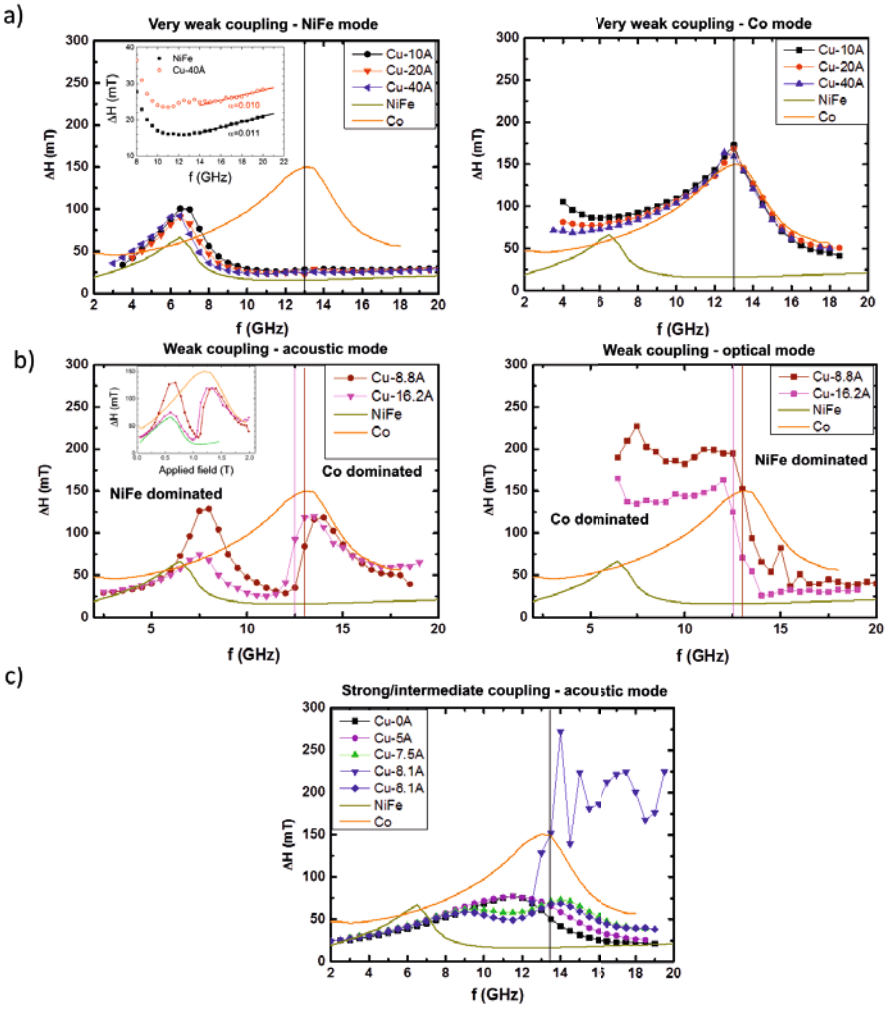

Figure 4.10: The frequency dependence of the linewidth (ΔH) for samples in different regimes. The inset in (a)left shows ΔH in the frequency range 8–22 GHz, together with a linear fit. The inset in (b)left shows ΔH as a function of field. The linewidth of the unidentified mode in Cu-8.1 Åis shown by blue triangles in (c).

4.2.5 Linewidth-frequency dependency characteristics of each regime

The linewidth of the single films is shown in Figure 4.10. Both NiFe and Co display large peaks in ΔH, but at different frequencies. The maximum in ΔH_{Co} coincides with the CP frequency by chance; the two are not directly related. The peak maxima of NiFe and Co occur at $\mu_0 H \approx 0.6$ and 1.2 T, which correspond to the magnetization angles $\theta_{\mathrm{int}} = 42°$ and 37°, respectively (see Fig. 4.5(c)). The calculated values correspond well with the expected $\theta_{\mathrm{int}} = 45°$, despite the simplicity of the model.

The overall shape of the $\Delta H(f)$ curves is preserved in the very weak coupling regime (Fig. 4.10(a)), and each mode closely follows the behavior of the respective single film. The inset in Figure 4.10(a) shows the linewidth of NiFe and Cu-40Å, together with a linear fit. The damping constant of both samples is similar, which implies that spin pumping effects are either ineffective in this frequency/field range or that the spin-sink efficiency of the Co and the cap layers is equal. The latter requires that the thickness of the top Cu layer is smaller than the spin diffusion length (λ_{sd}). However, λ_{sd} of the sputtered Cu films is small and the spin-pumping contribution to α decreases rapidly for $t_{\mathrm{Cu}} > 10$ Å[95]. This is confirmed by the in-plane measurements, since the damping constants are higher for the trilayers than for the single NiFe (Section 4.1). Furthermore, the frequency dependence of the in-plane linewidth clearly shows that the linewidth broadening is dominated by spin pumping effects, not two-magnon scattering. We must therefore conclude that spin pumping is suppressed above $\mu_0 H > 1.3$ T.

The evolution of $\Delta H(f)$ in the weak coupling regime reflects the transition from NiFe (Co) to Co (NiFe) dominated acoustic (optical) modes (Fig. 4.10(b)). The linewidths of the acoustic modes peak at the same field as for NiFe (see inset to Fig. 4.10(b)), implying that the coupling to the Co layer is too weak to change the field dependence of $\theta_{\mathrm{int}}^{\mathrm{NiFe}}$. The onset of the second peak corresponds to the minima in Δf—i.e., the position of the frequency gap. The linewidth increases rapidly above this point and decreases again when the transition is complete. The optical mode displays a sharp drop in the same frequency range. Before the CP, the linewidth of this mode is much larger than ΔH^{Co}—a clear sign of out-of-phase precession combined with spin pumping [100, 104, 97]. Likewise, the linewidth is enhanced compared to ΔH^{NiFe} after the CP.

The linewidth is the only parameter differentiating the samples with strong and intermediate coupling in this study. The strongly coupled layers display a single peak in ΔH (Fig. 4.10(c)), signifying a coherent rotation of the magnetization in both layers. The linewidth approaches the NiFe values at high frequencies. Unfortunately, it is not possible to determine whether the damping is lower or higher than in the single NiFe film, due to the limited field range. For intermediate coupling, the bimodal shape of ΔH shows that the magnetization rotation is neither coherent nor governed by the single layers. The magnetization direction must instead vary continuously throughout the layers, as in exchange springs [105].

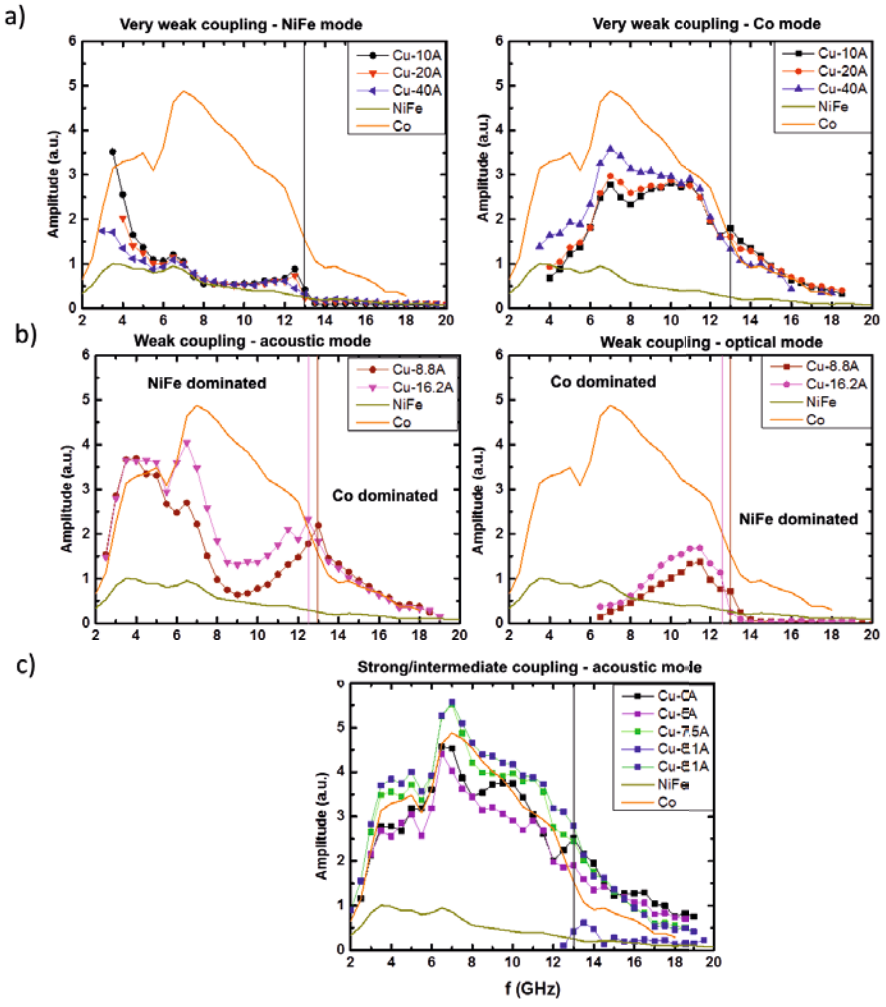

Figure 4.11: The amplitude of the absorption signal for samples belonging to different regimes. The linewidth of the unidentified mode in Cu-8.1 Åis presented by blue squares on a green line.

4.2.6 Amplitude-frequency dependency characteristics of each regime

The amplitude of an FMR signal and its frequency have a complex dependence on the properties of the measurement setup and the sample details. Nevertheless, if the data is

collected using the same setup, settings, and samples, the main contributions to a high amplitude are: a short distance to the source of the excitation field, a large total magnetic moment and (for multilayers) a large coupling strength [100]. The latter only holds for the acoustic mode; the optical mode shows an opposite trend and its intensity weakens. Figure 4.11 shows the amplitude as function of frequency, and the samples in each category again show similar behavior.

In the very weak coupling regime, a striking feature is observed as $f \to 0$: the intensity of the NiFe mode increases rapidly, while the Co mode declines, as shown in Figure 4.11(a). This hints of increased coupling between the layers. Moreover, the linewidth of the Co mode increases simultaneously and ΔH of the NiFe mode decreases faster than for the single film (Fig. 4.10(a)). Taken together with the in-plane data in Section 4.1, this can only be a sign of a transition to a collective precession. The origin of the emergence of collective modes is the so-called dynamic exchange coupling (DEC), which is generated by spin pumping and appears close to resonance coincidence points[106, 104, 97]. We use the notation CP to describe the resonance crossing at $f \approx 13$ GHz, but f^{NiFe} and f^{Co} also approach each other at low fields, allowing for the onset of dynamic exchange. The intensity of the NiFe mode increases slightly when the frequency comes close to the CP from below, while both modes closely follow the amplitude of the individual layers above the CP. This is consistent with the suppression of spin pumping at high frequencies and fields, as discussed above.

An evolution of the collective/individual nature of the modes can also be seen for the weak regime. The amplitude of the acoustic mode in the samples with weak IEC is high at low frequencies, while the optical mode is absent ($f^{\mathrm{op}}(H = 0) \approx 6$ GHz). The presence of dynamic exchange will thus not alter the nature of the precession, and it is not possible to detect the existence of DEC for $f \to 0$. However, the decline in this coupling with increasing frequency is clearly visible in Figure 4.11(b). The amplitude of the acoustic mode decreases above $f = 7$ GHz while the optical mode increases, in accordance with a lower effective coupling and a less collective behavior. At higher frequencies, the amplitude of both modes increases. This marks the onset of the transition between governing layers. The larger magnetic moment of the Co layer leads to a higher A compared to NiFe. Hence, the transition from NiFe-dominated to Co-dominated, as well as the more individual character of the optical/Co mode, will lead to an increase in A, as long as the optical mode is still mostly associated with the Co layer. There is no spin pumping above the CP and the acoustic mode has a high amplitude, whereas the A of the optical mode is smaller than for the single NiFe layer, as expected. The amplitude of the acoustic mode in samples belonging to the strong/intermediate regime is close to A_{Co} for the whole frequency range, as shown in Figure 4.11(c). It is therefore impossible to draw any firm conclusions about the DEC and the plausible mode transition. The acoustic nature of the mode is, however, evident.

4.2.7 Conclusion

In this study, the magnetic field was applied at an out-of-plane angle of 82° to facilitate a coincidence point where the resonance field and frequency of Co and NiFe are equal. I ob-

served three distinctly different regimes in coupling strength: very weak ($J' < 0.02$ mJ/m^2), weak ($J' \approx 0.1$ mJ/m^2), and intermediate/strong ($J' > 0.8$ mJ/m^2). The resonance fields closely followed the single-layer behavior for samples with very weak coupling (t_{Cu} = 10-40 Å). However, both linewidth and amplitude showed deviations at low frequencies. I attribute these changes to the dynamic exchange coupling that emerges when the FMR frequencies of two magnetic layers, subject to mutual spin pumping, approach each other. The impact of this coupling was also clear when $J' \approx 0.1$ mJ/m^2, and I have shown that the presence of the dynamic coupling always promotes a collective precession. Furthermore, the results imply that spin pumping is suppressed at high frequencies.

The modes in samples with weak IEC (t_{Cu} = 16.2 and 8.8 Å) had a distinct acoustic and optical nature. Close to the coincidence point, the two modes experienced a frequency gap—a hallmark of static interlayer coupling. The anticrossing was accompanied by a transition of the governing layer for the modes, as unambiguously revealed by the linewidths and amplitudes: Below the CP, NiFe dominates the acoustic mode and Co dominates the optical mode; above the CP, the situation is reversed and Co dominates the acoustic mode, while NiFe governs the optical mode.

Only the acoustic mode was observed in samples with strong/intermediate coupling. The field dependence of the linewidth showed that the layers behave as a single film for $t_{\mathrm{Cu}} \leq 5$ Å, while the magnetization in layers separated by a thicker spacer is exchange-spring like.

4.3 Effect of microwave current on resonances of coupled Py/Cu/Co trilayers in oblique magnetic fields

In this work, we use the ST-FMR technique to study the effect of the rf current on the magnetodynamics in the vicinity of the coincidence point of the NiFe/Cu/Co multilayers. We chose spacer layers thick enough to avoid the RKKY interaction between the two FM layers: that is, thicknesses of 2 nm and 8 nm, with the latter being a reference for the former.

In particular, we investigate two distinct regimes: (a) decoupled, by using a sufficiently thick Cu layer of $t_{Cu} = 8$ nm to avoid the RKKY interaction between the two FM layers and (b) weakly coupled, for $t_{Cu} = 2$ nm, using the former as reference to study the latter.

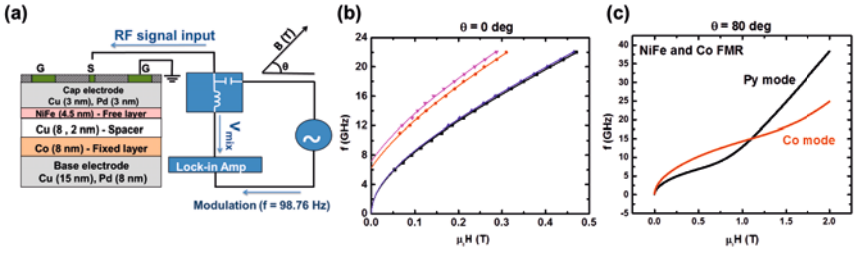

Figure 4.12: (a) Layout of the NC-STO and the spin torque FMR (ST-FMR) measurement setup. (b) Frequency vs. in-plane field dependence of the Co and Py FMR peaks for the samples with Cu spacer layer thickness of 8 nm and 2nm. (c) Simulated Co and Py FMR frequencies versus strength of the magnetic field at $\theta = 80°$ out-of-plane.

4.3.1 Sample layout and experimental setup

The layout of the NC-STO is demonstrated in Figure 4.12 (a); NCs of nominal diameter 400 nm are defined through the SiO_2 insulating layer using e-beam lithography at the center of the mesa. We chose a relatively large NC to reduce the linewidth and asymmetry of the excited peaks caused by the excitation of the SWR.

All measurements were performed at room temperature in a custom-built probe station utilizing a uniform magnetic field of up to 2 T. Our ST-FMR measurements schematic is shown in Figure 4.12 (a) and details can be found in Section 2.2.3.

4.3.2 Characterization of samples in in-plane field configuration

We first characterized our samples using in-plane applied fields. For this purpose, we chose a spacer layer thick enough to suppress any means of the coupling between the layers, to ensure they behave similarly to free-running films. The FMR frequency dependencies are

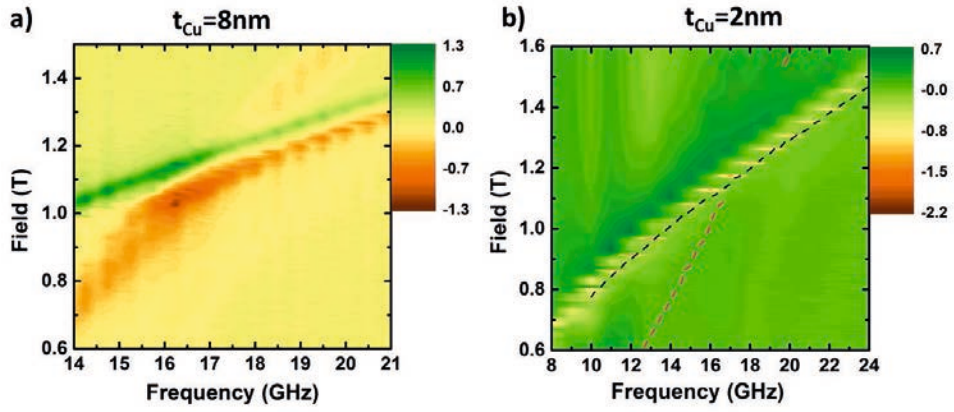

Figure 4.13: Colormaps represent the field vs. frequency dependence of the mixing voltage measured for a) t_{Cu} = 8 nm and b) t_{Cu} = 2 nm for the applied field at $\theta = 80°$ out-of-plan. The black and red dashed lines show the FMR of the Py and Co layers extracted from the t_{Cu} = 8 nm sample.

fitted using Equation (2.3). The results of this fit are shown in Figure 4.12b and the values of the extracted parameters are summarized in Table 4.1.

	Thickness of spacer, nm	$\mu_0 M_s$, T	γ, GHz / T	$\mu_0 H_{add}$, mT
Py	8	0.746	29	0
Co	8	1.100	31	0
Py	2	0.746	29	0.032
Co	2	1.100	31	0.110

Table 4.1: Summary of magnetic parameters extracted from fitting the in-plane ST-FMR data to the Kittel model.

4.3.3 Characterization of samples in out of plane angle of the field

Using Equation (2.4) and (2.5), we then calculate how the FMR frequencies behave with the field applied $\theta = 80$ out-of-plane.

The results of this calculation are shown in Figure 4.12c. We observe that Co and Py FMRs curves cross at the frequency and resonance field of around $f = 15$ GHz and $\mu_0 H = 1.2$ T, respectively. In fact, our ST-FMR measurements on the $t_{Cu} = 8$ nm sample (see Fig. 4.13a) are in good agreement with the theoretical estimate.

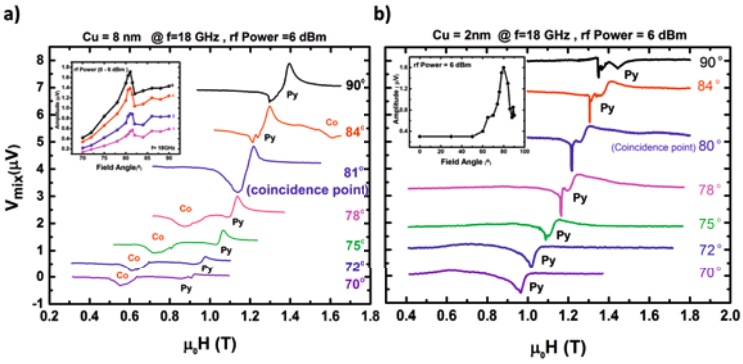

Figure 4.14: ST-FMR spectra of the samples with spacer thickness of (a) 2 nm and (b) 8 nm, acquired at a fixed rf current frequency of 18 GHz for different applied field angles. Insets show fitted amplitude of the observed resonances.

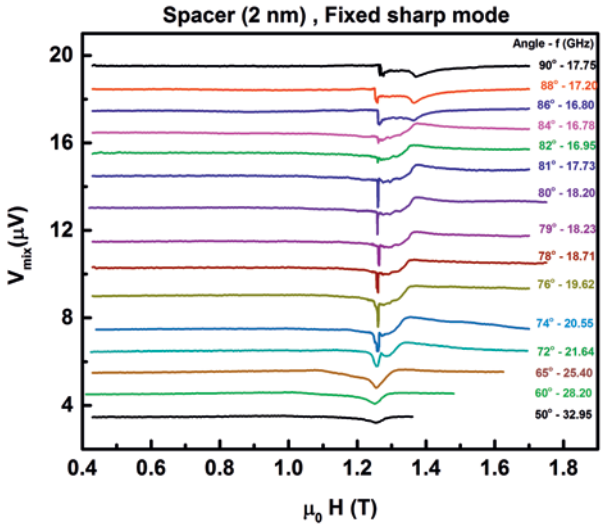

Figure 4.15: ST-FMR spectra of the sample with the Cu spacer thickness of 2 nm measured so as to keep the resonance field of the sharp peak constant. This demonstrates how the resonance field difference with the FMR mode increases with the applied field angle.

Figure 4.13a shows that there is neither anticrossing nor reduction of the linewidth of the peaks at the coincidence point, consistent with our regular FMR measurements. This again

confirms virtually the decoupled dynamics of the layers and suggests a vanishing dynamic exchange coupling[107]. The observed increase of the mixing voltage at the coincidence point happens as the dc signals of both layers add up. It is worth noting that the Py and Co peaks have significantly different line shapes. According to Kupferschmidt et al. [108], a symmetric lineshape of the Co FMR suggests that it is detected via the spin-pumping effect, while the antisymmetric shape of the Py FMR highlights the dominance of the spin-diode effect. This difference suggests much stronger spin current injection from Co to Py than the other way around.

The situation is substantially different for $t_{Cu} = 2$ nm. We can no longer resolve the Co FMR in the measured frequency range; instead, we observe a broad Py FMR peak accompanied by a rather sharp mode shifted to higher frequencies (see Fig. 4.13b). Both go virtually in parallel with the rf frequency, suggesting that the sharp peak originates from the Py layer.

The same qualitative behavior is observed for both Cu thicknesses when we fix the frequency of the ST-FMR and instead sweep the applied field angle (see Fig. 4.14). In this case, however, the sharp mode only appears in the vicinity of the coincidence point, starting at roughly 75. If we now change the frequency of the microwave current, we can observe the mode in the much broader range of applied field angles. For the sake of comparison, we perform our measurements in a way that the sharp mode has roughly the same resonance field. To do this, for the given angle of the applied field of $\mu_0 H = 1.26T$, we performed a frequency sweep measurement to find the exact position of the sharp peak. We then carried out a field sweep measurement at the same frequency as the sharp peak, as shown in Figure 4.15. This plot reveals how the sharp peak appears in the vicinity of the Py FMR, starting from an applied field angle of roughly 60. As the angle increases to 80, the linewidth of the sharp mode drops significantly to $\mu_0 \Delta H = 0.8$ mT, and the FMR moves away from it to higher fields. As we increase the angle further, the distance between the two modes remains virtually the same (around 0.1 T), while the linewidth of the sharp mode gradually increases.

4.3.4 Discussion

To understand the nature of the sharp mode, we first note that, irrespective of the applied field angle and microwave frequency, this mode appears above the Py FMR mode. As we seen before, a weak positive coupling between the layers might transform the FMR modes of the individual layers to the collective resonances that are shifted to the higher frequencies (see Section 4.1). However, the splitting between the sharp and broad peaks at the coincidence point is (a) too large to be attributed to the weak RKKY interaction at $t_{Cu} = 2$ nm and (b) cannot be related to the dynamic exchange coupling, as it should remain virtually the same for $t_{Cu} = 8$ nm (i.e., it decays substantially only if the Cu spacer thickness is on the order of its spin diffusion length of 100 nm–1 μm[109]). Furthermore, as both modes show virtually the same frequency vs. field slope, they should belong to the same magnetic layer (Py in this case).

In fact, the sharp mode is observed in the band of the propagating spin waves, similar

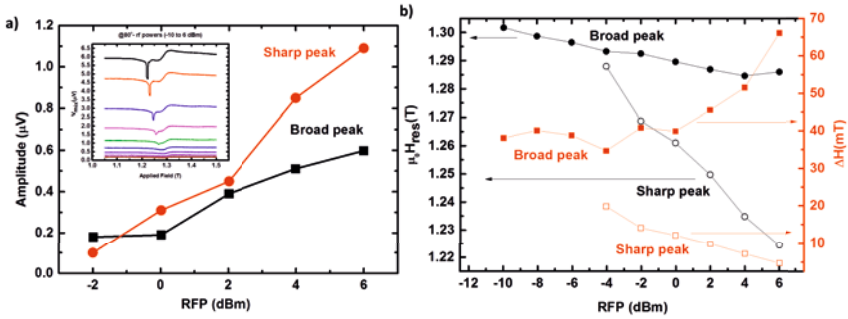

Figure 4.16: (a) ST-FMR spectra versus rf current power of the sample with 2 nm spacer layer and (b) the corresponding fitted resonance fields and linewidths of the sharp and FMR modes.

to the Oersted-field-driven SWR we found for the magnetic field applied in-plane. The substantial difference, however, is that we found a mean linewidth for the Oersted-driven FMR and SWRs of around 15 mT and 25 mT, respectively, for the NC diameter of 240 nm and a microwave frequency of 18 GHz. The observed sharp peak is thus much narrower than the typical linewidth of the linear resonances and cannot therefore be attributed to the more coherent linear excitation of SWs, due (for example) to the larger NC diameter. So there should instead be some antidamping mechanism at play that reduces the intrinsic magnetic losses beneath the nanocontact.

To reveal the properties of this mechanism, we measure how the response of the system evolves with the applied current power, as shown in Figure 4.16a. Both the FMR and the sharp mode exhibit nonlinear behavior. In particular, both types of resonance experience blueshifting of their resonance frequencies, suggesting positive nonlinearity. This is consistent with the theoretical estimations for the similar Py film[64], as in our case Py is saturated at 80 out-of-plane, which is well above the linear magnetization angle of $\theta \approx 60$ at which the nonlinearity turns from negative to positive.

While moderate changes of the FMR resonance field and substantial increase of its linewidth might be attributed to the nonuniform Joule heating[110], this would not explain why the sharp mode experiences significantly larger blue-shifting and, most importantly, a dramatic reduction of its linewidth (see Fig. 4.16b). At the same time, for sufficiently large applied currents, the rf Oersted field might drive Py modes to the nonlinear regime where the so-called Suhl instabilities emerge[111]. Although this could explain the growth of the amplitude and the corresponding blueshifting of both the FMR and the sharp modes, such kind of auto-oscillations typically lead to a foldover effect[112, 113], which we do not observe in our ST-FMR measurements. Furthermore, we expect the rf Oersted field to drive the FMR much more strongly than any SWR modes, so it should have a steeper resonance field vs. current dependence than the propagating mode. Finally, in contrast to our observations, the Oersted-field-induced effects should be virtually independent of the

position of the Co peak.

The only possibility to explain the sharp peak thus involves spin transfer torque. Indeed it might excite auto-oscillations even with rf currents—that is, parametrically[114]. However, the microwave signal might only excite at either its half or double frequencies, i.e. 9 GHz or 36 GHz, respectively for 18 GHz pumping. The former is unlikely, as such resonances would lie below FMR of both Py and Co for the given applied fields; the second option should appear at a much larger shift from the FMR than we observe experimentally. As with the Oersted field, we would also expect such parametric pumping to be independent of the position of the Co peak.

At the same time, a direct spin current might provide antidamping and, in our particular case of positive nonlinearity, lead to the nucleation of propagating spin waves, the so-called Slonczewski mode[115]. Although this might sound counter-intuitive, since we drive our system with rf currents, we would like to stress again that the resonances are detected partially due to the spin-pumping effect—that is, a dc current that magnetization dynamics injects into the adjacent metallic layers. The magnitude of this effect is proportional to the magnetization precession amplitude. In particular, we expect it to be much reduced in the Co layer for the spacer thickness of $t_{Cu} = 8$ nm, as most of the rf current will flow through Cu and the amplitude of the rf Oersted field at the Co cite will decreased.

The spin pumping from Co to Py layer should happen whenever the Co dynamics is driven, so it should potentially drive magnetization auto-oscillations in Py even when resonances of both magnetic layers are separated from each other. However the nature of the ST-FMR measurements does not allow us to track dynamics of both layers simultaneously. So if the resonances of FMR layers are well separated, there will be no spin pumping from the Co layer once we tune to the Py modes and vice versa. It is thus only by bringing the resonance conditions of both layers together that we can observe the effect of antidamping.

Finally, we would like to emphasize that the observed blueshifting of the sharp mode might only occur in case of auto-oscillation. We thus conclude that spin pumping from the Co layer to the Py layer is sufficient to fully compensate magnetic losses beneath the NC.

4.3.5 Conclusion

I have observed a sharp feature at the resonance frequency of the coupled pseudo-spin-valve excited by rf current. The mode appears in the Py layer and experiences significant blueshifting of its frequency with applied current strength, consistent with positive nonlinearity of the NiFe film. Nucleation of the self-sustained propagating spin waves (Slonczewski mode) via rf-to-dc current conversion can be demonstrated. In particular, as I drive magnetization dynamics in Co and Py layers with rf current, and thus Oersted fields, it creates a mutual DC current injection via the spin-pumping effect. This provides mutual antidamping and, for sufficiently strong rf powers, leads to the nucleation of the magnetization auto-oscillations. As the magnetization dynamics at the same frequency are pumped and detected, the linewidth reduction and auto-oscillations might only be observed in the vicinity of the Py and Co resonances crossing. In this case, I detected a sharp peak with a linewidth as small as $\mu_0 \Delta H = 0.8$ mT, and this could be reduced further with

higher rf current amplitudes and thinner Cu spacer layers. In fact, I observed that the auto-oscillations disappear for $t_{Cu} = 8$ nm, consistent with the reduction of the Oersted field amplitude at the Co site and suppression of the spin diode effect due to the lateral current spread.

Chapter 5

Conclusions and future works

Conclusions

The research presented in this thesis has centered on fundamental Spintronics research on the pseudo-spin-valve (pSV) structure in the form of blanket film and nanocontact (NC) geometry. The main focuses were on studying the nature of the excited spin-wave resonances in in-plane magnetized NC pSVs by means of the ST-FMR technique, and the study of magnetodynamics in coupled pSVs in in-plane and out-of-plane applied fields by means of broadband conventional FMR and ST-FMR techniques. The following is a list summarizing all the results:

Results from the study of spin waves in in-plane magnetized NC-STOs on Co/Cu/Py pSVs in two sections:

1. For in-plane fields, it is the the rf Oersted field in the vicinity of the NC that plays the dominant role in generating the observed spectra, and not the STT.

2. In addition to the FMR mode, exchange dominated spin waves are also generated.

3. The NC diameter sets the mean wavevector of the exchange dominated spin wave, in good agreement with the expected dispersion relation.

4. By changing the spread of the lateral current, the spatial characteristics of the resulting spin-wave beams can be controllably tuned.

5. The effective diameter (inversely proportional to the mean wavevector) decreases when the Cu bottom layer thickness is increased.

Results from the study of interlayer exchange coupling between FM layers in Co/Cu(t)/Py pSVs in three sections:

1. It is possible to engineer a cut-off frequency, using the strength of the IEC, below which spin pumping is minimized.

1. By applying the magnetic field at an out-of-plane (OOP) angle, a coincidence point where the resonance field and frequency of both FM layers are equal is facilitated. Due to behaviour of governing layer around coincidence point, three distinctly different regimes are observed in coupling strength: very weak or single layer behavior ($J' < 0.02$ mJ/m^2), weak or collective behavior ($J' \approx 0.1$ mJ/m^2) and intermediate/strong or alloy-like behavior ($J' > 0.8$ mJ/m^2).

2. In OOP configuration, the modes in samples with weak IEC had a distinct acoustic and optical nature. Close to the coincidence point, the two modes experienced a frequency gap due to a transition of the governing layer for the modes.

3. In strong/intermediate coupling regime, the field dependence of the linewidth showed that the layers behave as a single film for $t_{\mathrm{Cu}} \leq 5$ Å, while the magnetization in layers separated by a thicker spacer is exchange-spring like.

1. Exciting coupled NC pSVs by rf current in the OOP configuration results in a high Q=factor peak with a linewidth as small as $\mu_0 \Delta H = 0.8$ mT in the vicinity of resonance coincidence point.

2. The mode appears in the Py layer and experiences significant blueshifting of its frequency with applied rf current strength, consistent with positive nonlinearity of the Py film. Nucleation of the self-sustained propagating spin waves (Slonczewski mode) can be demonstrated via rf-to-dc current conversion.

3. This feature disappears for $t_{Cu} = 8$ nm, consistent with the reduction of the Oersted field amplitude at the Co site and suppression of the spin diode effect due to the lateral current spread.

Future works

ST-FMR study of frequency doubling in NCs on Heusler alloys

During my study of NCs, described in Chapter 3, I found there is a lack of fundamental studies of these geometries. For example, in the low-frequency field range, double frequency mode could be excited and detected easily by ST=FMR technique in NCs, and nonlinearity empowers the modes. Heusler alloys are good materials to investigate in NC geometry through the excitation of double frequency modes, as the effectiveness of double frequency modes is proportional to the ellipticity of the magnetization and is most sensitive in samples with transverse demagnetization factors that are not equal to each other[7]. The method can thus serve as a good probe for studying magnetodynamics in Heusler materials.

FMR study of exchange coupling in FM/NM (t)/FM trilayers with different NM materials in the vicinity of the coincidence point

Exchange coupling between layers and acoustic and optical modes remains a subject of active research. Clear observation of both the acoustic and optical behavior of the modes and the tracking of the contribution of the governing layers (see Section 4.2) may lead to more complex studies that involve different spacer layers, such as Ru or topological insulators. This can also be further investigated through cryo-FMR at ultralow temperatures.

ST-FMR study of the sharp feature in coupled FM/NM (t)/FM trilayers with different NM and FM materials

Observation of sharp features by means of rf current is reported here for the first time in an NC geometry on a pseudo-spin-valve structure. There is much opportunity to continue this work experimentally by choosing different materials for the spacer layer, or even by changing the materials of ferromagnetic layers and going deeper into the nature of the mode from the theoretical point of view.

Bibliography

[1] F. Bloch, Zeitschrift für Physik **61**, 206 (1930).

[2] G. Heller and H. A. Kramers, Proceedings Koninklijke Akademie van Wetenschappen **37**, 378 (1934).

[3] V. G. B. A. I. Akhiezer and S. V. Peletminskii, Science **163**, 923 (1969).

[4] W. Marshall and S. W. Lovesey, Science **77**, 50 (1972).

[5] D. D. Stancil, *Theory of Magnetostatic Waves* (Springer New York, 1993).

[6] C. Kittel, *Introduction to Solid State Physics* (Wiley, 1996).

[7] G. A. Gurevich, A. G. &Melkov, *Magnetization Oscillation and Waves* (CRC press, 1996).

[8] M. G. Gottam, *Linear and Nonlinear Spin Waves in Magnetic Films and Superlattices* (World scientific publishing co. Pte. Ltd., 1994).

[9] A. V. Chumak, V. I. Vasyuchka, A. A. Serga, and B. Hillebrands, Nat. Phys. **11**, 453 (2015).

[10] M. G. Kottam and D. J. Lockwood, *Light Scattering in Magnets* (Nauka, 1994).

[11] J. C. Slonczewski, J. Magn. Magn. Mater. **159**, L1 (1996).

[12] M. Tsoi, A. G. M. Jansen, J. Bass, W.-C. Chiang, M. Seck, V. Tsoi, and P. Wyder, Phys. Rev. Lett. **80**, 4281 (1998).

[13] W. Rippard, M. Pufall, S. Kaka, T. Silva, and S. Russek, Phys. Rev. B **70**, 100406 (2004).

[14] W. H. Rippard, M. R. Pufall, S. Kaka, S. E. Russek, and T. J. Silva, Phys. Rev. Lett. **92**, 027201 (2004).

[15] G. Gerhart, E. Bankowski, G. A. Melkov, V. S. Tiberkevich, and A. N. Slavin, Phys. Rev. B **76**, 024437 (2007).

[16] M. Jamali, J. H. Kwon, S.-M. Seo, K.-J. Lee, and H. Yang, Sci. Rep. **3**, 3160 (2013).

[17] B. Lenk, H. Ulrichs, F. Garbs, and M. M?nzenberg, Phys. Rep. **507**, 107 (2011).

[18] S. Dutta, D. E. Nikonov, S. Manipatruni, I. A. Young, and A. Naeemi, IEEE Trans. Magn. **50**, 1 (2014).

[19] R. K. Dumas, E. Iacocca, S. Bonetti, S. R. Sani, S. M. Mohseni, A. Eklund, J. Persson, O. Heinonen, and J. Åkerman, Phys. Rev. Lett. **110**, 257202 (2013).

[20] S. Mangin, M. Gottwald, C.-H. Lambert, D. Steil, V. Uhlr, L. Pang, M. Hehn, S. Alebrand, M. Cinchetti, G. Malinowski, Y. Fainman, M. Aeschlimann, and E. E. Fullerton, Nat. Mater. **13**, 286 (2014).

[21] J. F. Bobo, L. Gabillet, and M. Bibes, J. Phys.: Condens. Matter **16**, S471 (2004).

[22] C. Kittel, Phys. Rev. **110**, 1295 (1958).

[23] P. Grünberg, R. Schreiber, Y. Pang, M. B. Brodsky, and H. Sowers, Phys. Rev. Lett. **57**, 2442 (1986).

[24] R. Urban, G. Woltersdorf, and B. Heinrich, Phys. Rev. Lett. **87**, 217204 (2001).

[25] Y. Tserkovnyak, A. Brataas, and G. E. W. Bauer, Phys. Rev. Lett. **88**, 117601 (2002), 0110247.

[26] B. Heinrich, Y. Tserkovnyak, G. Woltersdorf, A. Brataas, R. Urban, and G. E. W. Bauer, Phys. Rev. Lett. **90**, 187601 (2003), 0210588.

[27] A. A. Baker, A. I. Figueroa, C. J. Love, S. A. Cavill, T. Hesjedal, and G. Van Der Laan, Phys. Rev. Lett. **116**, 1 (2016).

[28] G. B. G. Stenning, L. R. Shelford, S. A. Cavill, F. Hoffmann, M. Haertinger, T. Hesjedal, G. Woltersdorf, G. J. Bowden, S. A. Gregory, C. H. Back, P. A. J. de Groot, and G. van der Laan, New J. Phys **17**, 013019 (2015).

[29] J. Lindner and K. Baberschke, J. Phys.: Condens. Matter **15**, R193 (2003).

[30] A. Layadi, Phys. Rev. B **65**, 104422 (2002).

[31] Y. Wei, S. Jana, R. Brucas, Y. Pogoryelov, M. Ranjbar, R. K. Dumas, P. Warnicke, J. Åkerman, D. A. Arena, O. Karis, and P. Svedlindh, J. Appl. Phys. **115** (2014).

[32] A. F. Franco and P. Landeros, J. Phys. D: Appl. Phys. **49**, 385003 (2016).

[33] Y. S. Joe, A. M. Satanin, and C. S. Kim, Phys. Scr. **74**, 259 (2006).

[34] J. Göres, D. Goldhaber-Gordon, S. Heemeyer, M. A. Kastner, H. Shtrikman, D. Mahalu, and U. Meirav, Phys. Rev. B **62**, 2188 (2000).

[35] A. R. P. Rau, Phys. Scr. **69**, C10 (2004).

[36] T. J. Silva and W. H. Rippard, J. Magn. Magn. Mater. **320**, 1260 (2008).

[37] S. Bonetti, P. Muduli, F. Mancoff, and J. Åkerman, Appl. Phys. Lett. **94**, 102507 (2009).

[38] R. Dumas, S. Sani, S. Mohseni, E. Iacocca, Y. Pogoryelov, P. Muduli, S. Chung, P. Dürrenfeld, and J. Åkerman, IEEE Trans. Magn. **50**, 4100107 (2014).

[39] S. Bonetti, V. Tiberkevich, G. Consolo, G. Finocchio, P. Muduli, F. Mancoff, A. Slavin, and J. Åkerman, Phys. Rev. Lett. **105**, 217204 (2010).

[40] V. E. Demidov, S. Urazhdin, and S. O. Demokritov, Nat. Mater. **9**, 984 (2010).

[41] M. Madami, S. Bonetti, G. Consolo, S. Tacchi, G. Carlotti, G. Gubbiotti, F. Mancoff, M. A. Yar, and J. Åkerman, Nat. Nanotechnol. **6**, 635 (2011).

[42] S. Bonetti, V. Puliafito, G. Consolo, V. S. Tiberkevich, A. N. Slavin, and J. Åkerman, Phys. Rev. B **85**, 174427 (2012).

[43] S. Sani, J. Persson, S. M. Mohseni, Y. Pogoryelov, P. Muduli, A. Eklund, G. Malm, M. Käll, A. Dmitriev, and J. Åkerman, Nat. Commun. **4**, 2731 (2013).

[44] S. R. Sani, P. Dürrenfeld, S. M. Mohseni, S. Chung, and J. Akerman, IEEE Trans. Magn. **49**, 4331 (2013).

[45] S. R. Sani, J. Persson, S. Mohseni, V. Fallahi, and J. Åkerman, J. Appl. Phys. **109**, 07C913 (2011).

[46] S. M. Mohseni, S. R. Sani, J. Persson, T. Anh Nguyen, S. Chung, Y. Pogoryelov, and J. Åkerman, Phys. Status Solidi RRL **5**, 432 (2011).

[47] S. M. Mohseni, S. R. Sani, J. Persson, T. N. A. Nguyen, S. Chung, Y. Pogoryelov, P. K. Muduli, E. Iacocca, A. Eklund, R. K. Dumas, S. Bonetti, A. Deac, M. A. Hoefer, and J. Åkerman, Science **339**, 1295 (2013).

[48] P. Muduli, O. Heinonen, and J. Åkerman, J. Appl. Phys. **110**, 076102 (2011).

[49] P. Muduli, Y. Pogoryelov, Y. Zhou, F. Mancoff, and J. Åkerman, Integr. Ferroelectr. **125**, 147 (2011).

[50] P. K. Muduli, Y. Pogoryelov, S. Bonetti, G. Consolo, F. Mancoff, and J. Åkerman, Phys. Rev. B **81**, 140408 (2010).

[51] A. Houshang, E. Iacocca, P. Dürrenfeld, S. Sani, J. Åkerman, and R. Dumas, Nat. Nanotechnol. **11**, 280 (2016).

[52] S. Neusser and D. Grundler, Adv. Mater. **21**, 2927 (2009).

[53] V. V. Kruglyak, S. O. Demokritov, and D. Grundler, J. Phys. D: Appl. Phys. **43**, 260301 (2010).

[54] R. Dumas, S. Sani, S. Mohseni, E. Iacocca, Y. Pogoryelov, P. Muduli, S. Chung, P. Dürrenfeld, and J. Åkerman, IEEE Trans. Magn. **50**, 4100107 (2014).

[55] S. Bonetti and J. Åkerman, Nano-contact spin-torque oscillators as magnonic building blocks, in *Magnonics*, pp. 177–187, Springer, 2013.

[56] M. N. Baibich, J. M. Broto, A. Fert, F. N. Van Dau, F. Petroff, P. Etienne, G. Creuzet, A. Friederich, and J. Chazelas, Phys. Rev. Lett. **61**, 2472 (1988).

[57] D. Backes, D. Bedau, H. Liu, J. Langer, and A. D. Kent, J. Appl. Phys. **111**, 07C721 (2012).

[58] J. Dou, M. J. Pechan, E. Shipton, N. Eibagi, and E. E. Fullerton, J. Appl. Phys. **113**, 17C115 (2013).

[59] E. Landau, L.D.; Lifshitz, Phys. Z. Sowietunion **8**, 153 (1935).

[60] D. Polder, Physica **15**, 253 (1949).

[61] V. Arkadyev, J. Russ. Phys.-Chem. Soc. (1912).

[62] J. H. E. Griffiths, Nat. **158**, 670 (1946).

[63] C. Kittel, Phys. Rev. **71**, 270 (1947).

[64] G. Gerhart, E. Bankowski, G. A. Melkov, V. S. Tiberkevich, and A. N. Slavin, Phys. Rev. B **76**, 024437 (2007).

[65] N. Mecking, Y. Gui, and C.-M. Hu, Phys. Rev. B **76**, 224430 (2007).

[66] G. Woltersdorf, *Spin-Pumping and Two-Magnon Scattering in Magnetic Multilayers*, PhD thesis, Simon Fraser University, 2004.

[67] J. Åkerman, Science **308**, 508 (2005).

[68] B. N. Engel, J. Åkerman, B. Butcher, R. W. Dave, M. DeHerrera, M. Durlam, G. Grynkewich, J. Janesky, S. V. Pietambaram, N. D. Rizzo, J. M. Slaughter, K. Smith, J. J. Sun, and S. Tehrani, IEEE Trans. Magn. **41**, 132 (2005).

[69] J. C. Sankey, P. M. Braganca, A. G. F. Garcia, I. N. Krivorotov, R. A. Buhrman, and D. C. Ralph, Phys. Rev. Lett. **96**, 227601 (2006).

[70] H. Xi, Y. Shi, and K.-Z. Gao, J. Appl. Phys. **97**, (2005).

[71] A. A. Tulapurkar, Y. Suzuki, A. Fukushima, H. Kubota, H. Maehara, K. Tsunekawa, D. D. Djayaprawira, N. Watanabe, and S. Yuasa, Nat. **438**, 339 (2005).

[72] J. C. Sankey, Y.-T. Cui, J. Z. Sun, J. C. Slonczewski, R. A. Buhrman, and D. C. Ralph, Nat. Phys. **4**, 67 (2008).

[73] H. Kubota, A. Fukushima, K. Yakushiji, T. Nagahama, S. Yuasa, K. Ando, H. Maehara, Y. Nagamine, K. Tsunekawa, D. D. Djayaprawira, N. Watanabe, and Y. Suzuki, Nat. Phys. **4**, 37 (2008).

[74] C. Wang, Y.-T. Cui, J. Z. Sun, J. A. Katine, R. A. Buhrman, and D. C. Ralph, Phys. Rev. B **79**, 224416 (2009).

[75] C. Wang, H. Seinige, and M. Tsoi, Low Temperature Physics **39**, 247 (2013).

[76] C. Wang, Y.-T. Cui, J. A. Katine, R. A. Buhrman, and D. C. Ralph, Nat. Phys. **7**, 496 (2011).

[77] A. R. Mellnik, J. S. Lee, A. Richardella, J. L. Grab, P. J. Mintun, M. H. Fischer, A. Vaezi, A. Manchon, E.-A. Kim, N. Samarth, and D. C. Ralph, Nat. **511**, 449 (2014).

[78] T. Staudacher and M. Tsoi, Thin Solid Films **519**, 8260 (2011).

[79] T. Staudacher and M. Tsoi, J. Appl. Phys. **109**, (2011).

[80] H. Seinige, C. Wang, and M. Tsoi, J. Appl. Phys. **117**, (2015).

[81] H. Seinige, C. Wang, and M. Tsoi, J. Appl. Phys. **115**, (2014).

[82] O. P. Balkashin, V. V. Fisun, I. A. Korovkin, and V. Korenivski, Low Temperature Physics **40**, 929 (2014).

[83] J. N. Kupferschmidt, S. Adam, and P. W. Brouwer, Phys. Rev. B **74**, 134416 (2006).

[84] A. A. Kovalev, G. E. W. Bauer, and A. Brataas, Phys. Rev. B **75**, 014430 (2007).

[85] A. Houshang, M. Fazlali, S. R. Sani, P. Dürrenfeld, E. Iacocca, J. Åkerman, and R. K. Dumas, IEEE Magn. Lett. **5**, 3000404 (2014).

[86] Y. Yin, F. Pan, M. Ahlberg, M. Ranjbar, P. Dürrenfeld, A. Houshang, M. Haidar, L. Bergqvist, Y. Zhai, R. K. Dumas, A. Delin, and J. Åkerman, Phys. Rev. B **92**, 024427 (2015).

[87] A. Vansteenkiste, J. Leliaert, M. Dvornik, M. Helsen, F. Garcia-Sanchez, and B. Van Waeyenberge, AIP Adv. **4**, (2014).

[88] S. Petit-Watelot, R. M. Otxoa, and M. Manfrini, Appl. Phys. Lett. **100**, (2012).

[89] A. G. Gurevich and G. A. Melkov, *Magnetization Oscillations and Waves* (CRC Press, Boca Raton, FL, 1996).

[90] S. A. H. Banuazizi, S. R. Sani, A. Eklund, M. M. Naiini, S. M. Mohseni, S. Chung, P. Dürrenfeld, B. G. Malm, and J. Akerman, Nanoscale **9**, 1896 (2017).

[91] M. Fazlali, M. Dvornik, E. Iacocca, P. Dürrenfeld, M. Haidar, J. Åkerman, and R. K. Dumas, Phys. Rev. B **93**, 134427 (2016).

[92] S. S. P. Parkin, Phys. Rev. Lett. **67**, 3598 (1991).

[93] L. Z. Z. Zhang and P. E. Wigen, Phys. Rev. B **50**, 6094 (1994).

[94] X. M. Liu, H. T. Nguyen, J. Ding, M. G. Cottam, and A. O. Adeyeye, Phys. Rev. B **90**, 064428 (2014).

[95] Y. Tserkovnyak, A. Brataas, G. E. W. Bauer, and B. I. Halperin, Rev. Mod. Phys. **77**, 1375 (2005).

[96] K. Lenz, T. Toliński, E. Kosubek, J. Lindner, and K. Baberschke, Phys. Status Solidi C Conf. **1**, 3260 (2004).

[97] K. Lenz, T. Toliński, J. Lindner, E. Kosubek, and K. Baberschke, Phys. Rev. B **69**, 1 (2004).

[98] A. A. Baker, A. I. Figueroa, D. Pingstone, V. K. Lazarov, G. van der Laan, and T. Hesjedal, Sci. Rep. **6**, 35582 (2016).

[99] C. Kittel, Phys. Rev. **73**, 155 (1948).

[100] B. Heinrich, *Exchange Coupling in Magnetic Multilayers* (Springer Berlin Heidelberg, Berlin, Heidelberg, 2008), pp. 185–250.

[101] P. J. H. Bloemen, M. T. Johnson, M. T. H. van de Vorst, R. Coehoorn, J. J. de Vries, R. Jungblut, J. aan de Stegge, A. Reinders, and W. J. M. de Jonge, Phys. Rev. Lett. **72**, 764 (1994).

[102] T. Luciński, F. Stobiecki, D. Elefant, D. Eckert, G. Reiss, B. Szymański, J. Dubowik, M. Schmidt, H. Rohrmann, and K. Roell, J. Magn. Magn. Mater. **174**, 192 (1997).

[103] S. Takahashi, Appl. Phys. Lett. **104** (2014).

[104] B. Heinrich, G. Woltersdorf, R. Urban, and E. Simanek, J. Appl. Phys **93**, 7545 (2003).

[105] E. E. Fullerton, J. Jiang, and S. Bader, J. Magn. Magn. Mater **200**, 392 (1999).

[106] B. Heinrich, Y. Tserkovnyak, G. Woltersdorf, A. Brataas, R. Urban, and G. E. W. Bauer, Phys. Rev. Lett. **90**, 187601 (2003).

[107] B. Heinrich, Y. Tserkovnyak, G. Woltersdorf, A. Brataas, R. Urban, and G. E. W. Bauer, Phys. Rev. Lett. **90**, 187601 (2003).

[108] J. N. Kupferschmidt, S. Adam, and P. W. Brouwer, Phys. Rev. B **74**, 134416 (2006).

[109] J. Bass and W. P. Pratt Jr, J. Phys.: Condens. Matter **19**, 183201 (2007).

[110] T. Staudacher and M. Tsoi, J. Appl. Phys. **109**, (2011).

[111] H. Suhl, J. Phys. Chem. Solids **1**, 209 (1957).

[112] Y. S. Gui, A. Wirthmann, and C.-M. Hu, Phys. Rev. B **80**, 184422 (2009).

[113] C. Wang, H. Seinige, and M. Tsoi, J. Phys. D: Appl. Phys. **46**, 285001 (2013).

[114] P. Dürrenfeld, E. Iacocca, J. Åkerman, and P. K. Muduli, Appl. Phys. Lett. **104**, 052410 (2014).

[115] J. Slonczewski, J. Magn. Magn. Mater **195**, 261 (1999).

List of Figures

List of Tables